The Imprinted *Igf2-Igf2r* Axis is Critical for Matching Placental Microvasculature Expansion to Fetal Growth

Ionel Sandovici[1,2,3,*], Aikaterini Georgopoulou[1,3,8], Vicente Pérez-García[3,4,5,8], Antonia Hufnagel[1], Jorge López-Tello[3], Brian Y.H. Lam[2], Samira N. Schiefer[1], Chelsea Gaudreau[2], Fátima Santos[3,4], Katharina Hoelle[1], Giles S.H. Yeo[2], Keith Burling[2], Moritz Reiterer[6,7], Abigail L. Fowden[3], Graham J. Burton[3], Cristina M. Branco[6,7,9], Amanda N. Sferruzzi-Perri[3,9] & Miguel Constância[1,2,3,10]*

[1]Department of Obstetrics and Gynaecology and National Institute for Health Research Cambridge Biomedical Research Centre, Cambridge CB2 0SW, United Kingdom

[2]University of Cambridge Metabolic Research Laboratories and MRC Metabolic Diseases Unit, Institute of Metabolic Science, Addenbrookes Hospital, Cambridge CB2 0QQ

[3]Centre for Trophoblast Research, Department of Physiology, Development and Neuroscience, University of Cambridge, Cambridge CB2 3EG, United Kingdom

[4]Epigenetics Programme, Babraham Institute, Cambridge CB22 3AT, United Kingdom

[5]Centro de Investigación Príncipe Felipe, Eduardo Primo Yúfera, 46012 Valencia, Spain

[6]Physiological Laboratory, Department of Physiology, Development and Neuroscience, University of Cambridge, Cambridge CB2 3EG, United Kingdom

[7]Centre for Cancer research and Cell Biology, Queen's University Belfast, Belfast BT9 7AE, United Kingdom

[8]These authors contributed equally

[9]These authors contributed equally

[10]Lead contact

*Correspondence: is299@cam.ac.uk or jmasmc2@cam.ac.uk

SUMMARY

In all eutherian mammals, growth of the fetus is dependent upon a functional placenta, but whether and how the latter adapts to putative fetal signals is currently unknown. Here we demonstrate, through fetal, endothelial, hematopoietic and trophoblast-specific genetic manipulations in the mouse, that endothelial and fetus-derived IGF2 is required for the continuous expansion of the feto-placental microvasculature in late pregnancy. The effects of IGF2 on placental microvasculature expansion are mediated, in part, through IGF2R and angiopoietin-Tie2/TEK signalling. Additionally, IGF2 exerts IGF2R-ERK1/2-dependent pro-proliferative and angiogenic effects on primary feto-placental endothelial cells *ex vivo*. Endothelial and fetus-derived IGF2 also plays an important role in trophoblast morphogenesis, acting through *Gcm1* and *Synb*. Thus, our study reveals a direct role for the imprinted *Igf2-Igf2r* axis on matching placental development to fetal growth and establishes the principle that hormone-like signals from the fetus play important roles in controlling placental microvasculature and trophoblast morphogenesis.

INTRODUCTION

The mammalian fetus is totally dependent upon the placenta for nutrients and oxygen. Little is known, however, about how placental functional capacity adapts to meet fetal demands for growth. As gestation progresses, the increase in fetal size requires higher levels of nutrients and consequently higher levels of supply *via* placenta. Depending on the species, placental surface area for nutrient exchange increases 5 to 15 fold between mid and late gestation (Fowden et al., 2006). This remarkable adaptation is likely to occur, at least in part, in response to fetus-derived signals, but this important principle remains untested.

We have previously proposed that imprinted genes play central roles in controlling both the fetal demand for, and the placental supply of, maternal nutrients (Constância et al., 2002, Constância et al., 2005, Coan et al., 2008, Angiolini et al., 2011). The *Igf2* (insulin-like growth factor 2) gene encodes a small polypeptide that is highly abundant in both fetal tissues and the fetal circulation. It is one of the most potent growth factors during intrauterine development, affecting the metabolism, proliferation, survival and differentiation of a wide variety of cell types (DeChiara et al., 1991, Baker et al., 1993, Gardner et al., 1999, Burns et al., 2001). In the mouse, homozygous mutants are indistinguishable from growth-deficient littermates with deletion of paternal *Igf2* allele, while mutants with a disrupted maternal *Igf2* allele are phenotypically normal (DeChiara et al., 1991). In humans, reduced *Igf2* expression contributes to the intra-uterine growth restriction in patients with Silver-Russell syndrome (SRS) (Azzi et al., 2014). Conversely, bi-allelic *Igf2* expression caused by loss of *Igf2* imprinting is observed in Beckwith-Wiedemann patients (BWS), a syndrome characterized by somatic overgrowth and increased predisposition to tumours (Azzi et al., 2014).

IGF2 exerts its effects by binding to several IGF/INS receptors (IGF1R, INSR, IGF1/INSR hybrids, IGF2R) (Sferruzzi-Perri et al., 2017). IGF2 binds to IGF2R with the highest affinity, which leads to either IGF2 degradation in the lysosomes or signalling via G-proteins (Okamoto et al., 1990, Maeng et al., 2009, Harris and Westwood, 2012). Additionally, IGF2R has further functions as a mannose 6-phosphate receptor (M6PR) and is also involved in the activation of latent transforming growth factor (TGF)-β1 (Ghosh et al., 2003). In the mouse, *Igf2r* is imprinted, being expressed only from the maternal chromosome (Barlow et al., 1991). Inactivation of the maternal *Igf2r* allele leads to body overgrowth (mutants are ~30% larger at birth) and perinatal lethality (Lau et al., 1994). This phenotype is largely caused by an excess of extra-cellular IGF2 as shown by the rescue of overgrowth with the introduction of an *Igf2* null allele (Wang et al., 1994). More recently, an IGF2 binding mutant allele (*Igf2r*^{I1565A}) was also shown to result in overgrowth and lethality (Hughes et al., 2019). In contrast, imprinting of *IGF2R* in the human is a polymorphic trait, with a minority of cases showing evidence for maternal expression in fetal and/or placental tissues (Xu et al., 1993, Oudejans et al., 2001, Monk et al., 2006).

Here, we apply genetic approaches to define the signalling mechanisms that allow communication between the fetus and placenta, by creating mouse models with a growth mismatch between the two. We first show that circulating IGF2 levels increase in late gestation, with a positive correlation to fetal size. We then provide evidence that endothelial and fetus-derived IGF2 is essential for the appropriate expansion of the feto-placental microvasculature and the underlying trophoblast in late gestation. We also find that endothelial-derived IGF2 plays an essential paracrine role on trophoblast morphogenesis. By contrast, trophoblast-derived IGF2 has only autocrine activities, without any impact on the feto-placental microvasculature. Our work demonstrates that the interaction of circulating IGF2 and endothelial IGF2 with the trophoblast is essential for matching the placental surface area for nutrient exchange to the growth rate of fetal tissues.

RESULTS

Expansion of Placental Labyrinthine Zone Coincides with Elevated Levels of Circulating and Endothelial IGF2

The gas and nutrient exchange layer of the mouse placenta (labyrinthine zone – Lz) increased in size with advancing gestational age (Figure 1A), matching the gain in fetal weight (Figure 1B). This is a specific effect of the Lz layer, as placental weight in mice decreases at the very end of gestation (Coan et al., 2004). Concomitantly, fetal plasma IGF2 increased approximately two-fold between E16 and E19 (Figure 1C). At these two developmental stages, we also observed a significant and positive correlation between fetal plasma IGF2 and fetal weights (Figure 1D). Within the placental Lz, *Igf2* expression was highest in feto-placental endothelial cells (FPEC) (Figure 1E) and its mRNA levels increased approximately six-fold between E14 and E19 (Figure 1F). *Igf2* ranked as the highest expressed gene in FPEC RNA-Seq transcriptome at E16, and several other known imprinted genes (Wei et al., 2014) ranked in the top one hundred out of approximately 14,000 genes detected (Figure 1G; Table S1). IGF2 protein was also highly expressed in FPEC (Figure 1H), and significantly higher than in the surrounding trophoblast cells (Figure 1I).

Fetal and Endothelial IGF2 Control Placental Lz Expansion

To explore whether fetus-derived IGF2 plays a direct role in placental development, we first used a conditional allele ($Igf2^{+/fl}$) to delete *Igf2* in the epiblast lineage using the $Meox2^{Cre}$ line (Tallquist et al., 2000) (Figures 2A and S1). The deletion of the paternally-inherited *Igf2* allele from embryonic organs and FPEC, but not extra-embryonic tissues, led to placental growth restriction from E14 onwards (Figure 2B). Stereological analyses indicated that only the placental compartments containing embryonic-derived structures (*i.e.* Lz and the chorionic plate – Cp) were smaller in the $Meox2^{Cre/+}$; $Igf2^{+/fl}$ mutants (referred subsequently as $Igf2^{EpiKO}$) (Figure 2C). The continuous expansion of the Lz, measured as volume increase between E14 and E19 was severely compromised in mutants (Figure 2C). The overall volume, surface area and total length of fetal capillaries (FC) were normal at E14, but became abnormal from E16 onwards (Figures 2D and S2A). Notably, all other components of the placental Lz, not originating from the embryonic lineage, *i.e.* labyrinthine trophoblast – LT, and maternal blood spaces – MBS, were also reduced in volume to a similar extent as the FC (Figure 2D). These findings provide evidence for a role of fetus-derived IGF2 on the expansion of placental Lz in late gestation.

IGF2 is highly expressed in FPEC, as previously shown (Figure 1E–I). Therefore, we next tested whether endothelial-derived IGF2 plays a role in placental development. Paternal *Igf2* allele deletion in the fetal endothelium, including FPEC, using the Tek^{Cre} line (Kisanuki et al., 2001) (Figures 2E and S3A–E) led to a moderate, but significant fetal and placental growth restriction, evident from E16 onwards (Figure 2F). Mutant $Tek^{Cre/+}$; $Igf2^{+/fl}$ (referred subsequently as $Igf2^{ECKO}$) placentae had reduced volumes of Cp and Lz at both E16 and E19 (Figure 2G), but less striking when compared to $Igf2^{EpiKO}$ mutants (Figure 2C). Within the Lz, the LT was reduced at both E16 and E19, while the MBS and FC were comparable to controls at E16, but significantly reduced at E19 (Figures 2H and S2B).

We next tested if IGF2 derived from hematopoietic cells (HC) contributed to the $Igf2^{ECKO}$ phenotype, and deleted the paternal *Igf2* allele in the hematopoietic lineage using the Vav^{iCre} line (de Boer et al., 2003). Efficient deletion of *Igf2* in HC (referred to subsequently as $Igf2^{HCKO}$, Figures S3F and S3G) did not have any significant impact on fetal and placental growth or on Lz expansion between E14 and E19 (Figure S3H). Additionally, $Igf2^{HCKO}$ mutant placentae had FC densities similar to that of controls at E19 (Figure S3I).

128 Although the 'small' Lz phenotype is observed in *Igf2*^{EpiKO} and *Igf2*^{ECKO} mutants only in later gestation,
129 it could originate as result of a reduced pool of multipotent labyrinth trophoblast progenitor (LaTP)
130 cells. LaTP cells are detected as clusters of EPCAM^{high} positive cells between E9.5 and E12.5 (Ueno et
131 al., 2013) (Figure 2I). Using flow cytometry analysis at E12, we found no significant difference in the
132 percentage of EPCAM^{high} positive cells between *Igf2*^{EpiKO} and *Igf2*^{ECKO} mutants and their corresponding
133 littermate controls (Figure 2J).

134 We conclude that the Lz phenotype observed in *Igf2*^{EpiKO} and *Igf2*^{ECKO} mutants is not the consequence
135 of a reduced pool of multipotent LaTP cells due to defective IGF2 signalling in early placental
136 development. However, our data cannot exclude defects in the differentiation potential of the
137 multipotent LaTP cells. The more severe impact on Lz growth observed in *Igf2*^{EpiKO} mutants compared
138 to *Igf2*^{ECKO} mutants also suggests that full placental Lz expansion in late gestation requires both fetus-
139 derived and endothelial-derived IGF2, but not hematopoietic-cell derived IGF2.

140

141 **Fetus-derived IGF2 Is Essential for Placental Morphogenesis and Microvasculature Expansion**

142 To uncover molecular signatures associated with the defective placental Lz expansion in *Igf2*^{EpiKO}
143 mutants, we performed an expression microarray analysis in micro-dissected Lz samples at E19, when
144 the Lz expansion and fetal demand for nutrients reach their maximum in absolute terms. Differentially
145 expressed genes (DEG) were enriched in genes implicated in vasculature development and immune
146 responses (Figures 3A, S4A and S4B). We identified a classic molecular signature of impaired
147 angiogenesis – reduced angiopoietin-Tie2/TEK signalling (Augustin et al., 2009) (Figure 3B; Table S2).
148 Lower levels of *Angpt1* and *Tek*, and increased expression of *Angpt2* were validated by qRT-PCR in an
149 independent set of biological samples at E19 and E16, but not at E14. (Figure 3B). Consistent with the
150 well-established roles of the angiopoietin-Tie2/TEK signalling in the control of endothelial cell survival
151 and proliferation (Augustin et al., 2009), placental TUNEL staining revealed a six-fold increase in
152 apoptotic cell frequency in mutants at E16, specifically in the Lz (Figure 3C). To explore directly the
153 identity of the apoptotic cells, we co-stained E16 *Igf2*^{EpiKO} mutant placentae for TUNEL and laminin, a
154 marker for the fetal capillary basement membrane (Milner et al., 1998). Our analysis revealed that the
155 majority of TUNEL+ cells (86.8 ± 4.25%) co-express laminin (Figure 3D), indicating that a large
156 proportion of the apoptotic cells are FPEC. Furthermore, endothelial cell proliferation measured by
157 flow cytometry was significantly reduced at E16 (Figures 3E and S4C), and this finding was confirmed
158 by immunofluorescence (Figure S4D).

159 In addition to vascular pathways (which, besides *Angpt1*, *Angpt2* and *Tek*, also include DEGs such as
160 *Dll4*, *Egfl6*, *Fzd4*, *Pdgfc* and *Slit2*, see Table S2), the expression microarrays also identified
161 transcriptional upregulation of genes related to immune responses and leukocyte migration (Figure
162 3A). Among these was *Adgre1*, a gene that encodes the glycoprotein F4/80, a highly specific cell-
163 surface marker for murine macrophages (Austyn and Gordon, 1981). The up-regulation of *Adgre1* was
164 confirmed by qRT-PCR in placental Lz also at E16 (Figure 3F). Immunostaining for F4/80 showed that
165 the total number of macrophages in Lz was significantly higher in mutants than controls (Figure 3G).
166 Additionally, clusters of macrophages surrounding feto-placental capillaries were found exclusively in
167 mutants (Figure 3G). Next, we assessed the impact of the described increased cell death, reduced cell
168 proliferation and macrophage infiltration, on capillary remodelling across gestation by CD31
169 immunostaining (marking endothelial cells). The density of FC was dramatically reduced at E16 and
170 E19, suggestive of a disproportionate loss of FPEC (Figure 3H). These CD31-stained or methylene blue-
171 stained resin sections also revealed small areas within the Lz of feto-placental capillaries with
172 accumulations of leucocytes but lacking endothelial cells, or obstructed and thrombotic capillaries

surrounded by disorganized and fragmented endothelial cells in late gestation (Figure S4E). Using electron microscopy, we did not observe evidence for feto-maternal barrier interruption that would allow for mixing between maternal and fetal blood, even in areas with disorganized FPECs (Figures S4F and S4G).

Importantly, the array data indicated downregulation of key genes involved in syncytiotrophoblast differentiation (*i.e. Gcm1* and *Synb* – which are expressed specifically in layer II of the syncytiotrophoblast, SynT-II, which is closest to FC; see Table S2). To validate these observations, we performed qRT-PCR and confirmed significant transcriptional reductions across late gestation of SynT-II-specific genes (Rawn and Cross, 2008, Nagai et al., 2010) *Gcm1*, *Synb* and *Slc16a3* (Figure 3I). However, only the SynT-I specific gene *Slc16a1* (Rawn and Cross, 2008, Nagai et al., 2010, Hughes et al., 2013) was modestly down-regulated, but not *Ly6e* and *Syna* (Figure S4H).

Together, our data show that lack of fetus-derived IGF2 triggers dysregulation of angiopoietin-Tie2/TEK signalling in late gestation, with consequent reduced FPEC proliferation and excessive cell death with associated placental macrophage infiltration. It also highlights that fetus-derived IGF2 supports normal development of the trophoblast cells, particularly the SynT-II layer, in a paracrine/endocrine manner, with a knock-on effect on the development of MBS.

Endocrine IGF2 Is a Fetus-derived Signal that Matches Placental Nutrient Supply Capacity to Fetal Demands for Growth

To provide further insights into the roles of fetus-derived IGF2 in matching placental and fetal growth we analysed five genetic models with either deletion of the paternal *Igf2* allele in fetal tissues, endothelium, trophoblast or ubiquitously, or overexpression of *Igf2* achieved through loss-of-imprinting in fetal tissues (Figure 4). For these models, we used flow cytometry to count FPEC, defined as $CD31^{+}/CD41^{-}$ cells (Rhodes et al., 2008 and Figures S5A–C), and measured Lz weight and circulating IGF2 levels. In $Igf2^{EpiKO}$ mutants, as expected from the immunostainings shown in Figure 3H, we observed a severe deficit in the total number and the proportion of FPEC at E16 and E19, but normal values at E14 (Figure 4A). The linear Lz expansion expected with gestational age was not observed in this model, matching the severe reductions in FPEC numbers and circulating IGF2 (Figure 4A). In contrast, in $Igf2^{ECKO}$ mutants lacking endothelial *Igf2*, circulating levels of IGF2 were only moderately reduced and total numbers of FPEC, but not relative numbers, were only significantly reduced at E19 (Figure 4B). Lz expansion in this model was only blunted at the end of gestation (Figure 4B). A deletion of *Igf2* specifically in the trophoblast cells of the placenta using $Cyp19^{Cre}$ (Wenzel and Leone, 2007) ($Igf2^{+/fl}$; $Cyp^{Cre/+}$ referred subsequently as $Igf2^{TrKO}$) (Figures 4C and S6A–E) did not result in changes in FPEC numbers and circulating IGF2, demonstrating that FPEC expansion is independent of trophoblast-derived IGF2. The rate of Lz expansion was normal in this model (Figure 4C). Ubiquitous deletion of *Igf2* in embryo and trophoblast using CMV^{Cre} (Schwenk et al., 1995) ($Igf2^{+/fl}$; $CMV^{Cre/+}$ referred subsequently as $Igf2^{UbKO}$) (Figures 4D and S6F) led to a loss of FPEC similar to that observed in the $Igf2^{EpiKO}$ mutants, further demonstrating that trophoblast-derived IGF2 does not contribute significantly to FPEC expansion. Lz weight was severely reduced from E14, in line with the near complete absence of IGF2 in fetal circulation (Figure 4D). Conversely, reactivating the transcriptionally silent maternal *Igf2* allele in $H19DMD^{fl/+}$; $Meox2^{+/Cre}$ mutants (Srivastava et al., 2000) (referred subsequently as *H19*-DMD^{EpiKO}) (Figures 4E, S6G and S6H), which led to increased levels of circulating IGF2, was associated with an increase of Lz weight and higher numbers of FPEC at E16 and E19 (Figure 4E). Taken together, these results show that IGF2 produced by fetal organs and secreted into the fetal

217 circulation stimulates the expansion of placental Lz, matching FPEC numbers to the fetal demand for
218 growth.

219

220 **IGF2 Signalling Controls Expression of FPEC-derived Angiogenic Factors**

221 To provide further molecular insights into the roles of fetal-derived IGF2 and FEPC-derived IGF2 on
222 microvasculature expansion, we carried out RNA-Seq analysis on FACS-isolated endothelial cells from
223 E16 placental Lz of *Igf2*^{EpiKO} and *Igf2*^{ECKO} mutants and their corresponding controls (Figures 5 and S5C
224 and S5D). Gene ontology (GO) analysis of DEGs identified in *Igf2*^{EpiKO} mutants showed statistical
225 enrichment of biological processes related to immune responses, cell migration, impaired cell
226 proliferation and angiogenesis, extracellular matrix organization and response to hypoxia (Figures 5A
227 and 5B; Table S3). We validated representative DEGs using qRT-PCR in independent biological samples,
228 including genes encoding proteins secreted by the endothelial cells into the extracellular space that
229 have known anti-angiogenic effects [*e.g.*, *Angpt2* (Augustin et al., 2009), *Adamts1* (Lee et al., 2006),
230 *Cxcl10* (Angiolillo et al., 1995) and *Thbs1* (Lawler et al., 2012)], factors implicated in cell migration and
231 response to hypoxia [*Edn1* (Lankhorst et al., 2016)], an interferon-response gene [*Iigp1* (Uthaiah et al.,
232 2003)], an inhibitor of cell proliferation [*Cdkn1a* (Vidal and Koff, 2000)] and a regulator of embryonic
233 vascular development [*Hey2* (Fisher et al., 2004)] (Figure 5C). Importantly, with the notable exception
234 of *Hey2*, all DEGs validated above in the *Igf2*^{EpiKO} model were also identified as DEGs in *Igf2*^{ECKO}
235 mutants, including the up-regulation of *Angpt2*, suggesting that these transcriptional changes are the
236 outcome of autocrine IGF2 actions on FPECs (Figure 5D; Table S3). Next, we searched for transcription
237 factor (TF) binding motifs enriched within the promoters of all DEGs found in the *Igf2*^{EpiKO} model. This
238 analysis identified significant enrichments for binding sites of four TFs encoded by DEGs – KLF4, EGR1,
239 IRF7 and HEY2 (Figure 5E; Table S3). Significantly, the four TFs control the expression of several
240 proteins involved in angiogenesis (labelled with * in Figure 5F and further presented in Table S4), some
241 of which are secreted by the endothelial cells into the extracellular space (Table S4). This analysis also
242 highlighted several chemokines that were up-regulated in FPEC [such as CCL2 (Gregory et al., 2006)
243 and IL15 (Fehniger and Caligiuri, 2001)] that are likely involved in attracting and modulating the activity
244 of macrophages that surround the feto-placental capillaries (as shown in Figure 3G). Thus, based on
245 our data, we propose that IGF2 signalling is necessary for proliferation and survival of FPECs.

246

247 **IGF2 Signalling on FPEC Is Mediated by IGF2R *in vitro* and *in vivo***

248 To further investigate the role of IGF2 in fetal capillary remodelling and identify the receptors that
249 might mediate its effects on endothelial cells, we isolated primary FPEC from E16 wild-type placental
250 Lz and cultured them *ex vivo* (Figures 6A, 6B and 6C). Only the type I (*Igf1r*) and type II (*Igf2r*) receptors
251 were expressed in FPEC both *in vivo* (Figure 6D) and *ex vivo* (Figure 6E). When cultured *ex vivo* for ten
252 days (passage one) FPEC switch off *Igf2* transcription, which differs from FPEC freshly isolated by FACS,
253 (Figure 6F). Exposure of cultured FPEC to exogenous IGF2 significantly increased their ability to form
254 capillary-like tube structures when seeded on matrigel (Figures 6G and 6H), demonstrating that IGF2
255 exerts direct angiogenic effects on FPEC. We also exposed cultured FPEC to IGF2^{Leu27}, an analogue
256 previously shown to bind to IGF2R with high selectivity (Beukers et al., 1991), which stimulated
257 capillary-like tube formation although to a lesser extent compared to IGF2 (Figures 6G and 6H). When
258 FPEC were treated with IGF2 and picropodophyllin (PPP), a small molecule that inhibits
259 phosphorylation of IGF1R without interfering with INSR activity (Girnita et al., 2004), their ability to
260 form capillary-like tube structures was very similar to that of cells treated with IGF2 alone (Figures 6G

261 and 6H). Thus, IGF2 exerts direct angiogenic effects on primary FPEC, which are mediated by IGF2R
262 and are independent of IGF1R.

263 To investigate further the observed effects of IGF2R in mediating IGF2 actions on primary FPECs, we
264 performed *Igf2r* knockdown using siRNA and investigated the impact on cell proliferation and
265 intracellular signalling with or without exogenous IGF2 stimulation (Figure 6I–L). Upon IGF2
266 stimulation, efficient *Igf2r* knockdown led to reduced FPEC proliferation, demonstrating that the pro-
267 proliferative actions of IGF2 on FPEC require IGF2R (Figure 6J). However, *Igf2r* knockdown also
268 resulted in reduced FPEC proliferation, even in the absence of IGF2 stimulation, suggesting that IGF2R
269 is required for normal FPEC proliferation, independent of IGF2 (Figure 6J). Additionally, FPEC
270 stimulated with IGF2 for 96 hours, but lacking IGF2R showed significant up-regulation of *Angpt2* mRNA
271 levels (Figure 6K). Acute IGF2 stimulation did not activate AKT, a key signalling node downstream of
272 IGF1R (Figure 6L). AKT phosphorylation was not affected by the IGF2R knockdown (Figure 6K).
273 However, we observed a significant delay in pERK1/2 phosphorylation upon acute stimulation of FPEC
274 with IGF2 (Figure 6K). These data demonstrate both IGF2-independent and IGF2-dependent actions
275 of IGF2R in controlling FPEC proliferation and highlight the role of ERK pathway in mediating the
276 actions of IGF2 on FPEC *via* IGF2R.

277 We further confirmed these *in vitro* findings using conditional deletions of IGF1R and IGF2R receptors
278 *in vivo*. Accordingly, efficient homozygous deletion of *Igf1r* from the endothelium (*Igf1r*^{ECKO}) did not
279 have any significant impact on fetal, whole placenta or placental Lz growth kinetics, nor did it alter the
280 total and relative numbers of FPEC/Lz, apart from a slight increase in the percentage of FPEC at E19
281 (Figures S7). Strikingly, the deletion of maternally-expressed *Igf2r* allele from the endothelium
282 (*Igf2r*^{ECKO} – see Figures 7A, 7B and 7C) resulted in a reduction in the percentage of FPEC/placental Lz
283 at both E16 and E19 (Figure 7D), further confirmed by a reduced density of CD31^{+} cells by
284 immunofluorescent staining (Figure 7E). The total number of FPEC/Lz was also significantly reduced at
285 E16, but became normal at E19 (Figure 7D). Notably, the overall placenta and Lz were overgrown,
286 from E16 onwards (Figures 7C and 7F), coincident with an increase in levels of circulating IGF2 in
287 plasma (Figure 7G). Together, our *in vitro* and *in vivo* experiments demonstrate that IGF2R mediates,
288 at least partially, the signalling actions of IGF2 on FPEC.

289

290 **DISCUSSION**

291

292 The major findings of this study are the identification of the imprinted *Igf2-Igf2r* axis as a key pathway
293 that controls the expansion of the placental vascular tree in late gestation, and the demonstration
294 that fetus-derived signals are important regulators of placental development and function. Although
295 a vast number of genetic pathways have been discovered that are important for the development of
296 different cell types in the placenta and the fetus, there are no functional genetic investigations to date
297 on how the fetus signals its nutrient requirements to the placenta and how the placenta matches
298 these demands (for example through the increase in surface area in late gestation). We tackled these
299 questions with an experimental design based on the manipulation of the growth rate of fetal tissues
300 independent of the placenta, and vice-versa, in the mouse. We used conditional targeting of imprinted
301 genes with well-established growth functions (*Igf2*, *Igf2r*, *H19*) as model systems (importantly, due to
302 imprinting, the mother is phenotypically normal). The analysis of these models of mismatch between
303 fetal and placental growth allowed us to establish a number of novel mechanistic principles that
304 regulate the cooperative signalling between the fetus and the placenta and, consequently, the control
305 of maternal resources.

306 Firstly, we found that circulating IGF2 correlates positively with fetal size in late gestation, reflecting
307 the growth rate of fetal tissues and the demand for nutrients. Mice with a severe decrease in levels of
308 circulating/fetal IGF2 showed a drastic (and disproportionate) loss of feto-placental endothelial cells.
309 This severe placental angiogenesis phenotype was associated with reduced endothelial cell
310 proliferation and increased apoptosis, altered differentiation of the underlying trophoblast and
311 reduced density of MBS, ultimately leading to a failure in the expansion of the Lz and surface area for
312 nutrient transport. Conversely, increased requirements for nutrients caused by bi-allelic *Igf2*
313 expression, which drove higher growth rates, led to 'overexpansion' of the Lz. Therefore, we show
314 that greater fetal demands for growth, driven by IGF2, signals enhanced placental growth. Secondly,
315 we also found that FPECs are a significant source of IGF2, with levels increasing with gestational age.
316 Endothelial *Igf2*-deficient mice show ~17% reduction in circulating IGF2 and impaired expansion of the
317 microvasculature and Lz, but no disproportionate reduction in number of FPECs (which is only seen
318 when circulating IGF2 is severely reduced). These findings strongly suggest that hormone-like signals
319 from the fetus, such as IGF2, are also required for the normal expansion of the Lz and surface area of
320 the placenta. Importantly, we ruled out the hypothesis that failure in expansion is due to a reduction
321 in the number of LaTP. IGF2 has been reported to be an essential component of maintenance of stem-
322 cell niches in other organs (Ferron et al., 2015, Ziegler et al., 2019). Our data suggest that endothelial
323 IGF2 and circulating IGF2 are not required for the proliferation and maintenance of LaTP pools, but
324 rather their differentiation.

325 Based on the experimental evidence provided in this study, we propose a model (Figure 7H) in which
326 fetus-derived IGF2, from multiple tissues, is the signal that allows matching placental supply capacity
327 to the fetal demands for growth. At the placental interface, circulating IGF2 directly stimulates
328 endothelial cell proliferation and survival, and capillary branching in part through IGF2R (as shown *in*
329 *vivo* and *ex vivo*). Circulating IGF2 may also directly control the growth and differentiation of the
330 underlying trophoblast, as it can cross (in free form or in binary complexes) the capillary walls or
331 permeate through the fenestrated endothelium (Bach, 2015). We suggest that the feto-placental
332 endothelium is a large reservoir of IGF2, boosting further IGF2 signalling, and acting in a paracrine and
333 autocrine manner to control the growth and remodelling of fetal capillaries, with a 'secondary effect'
334 on trophoblast morphogenesis. On the contrary, hematopoietic cells that originate from precursors
335 common to FPECs (Rhodes et al., 2008) do not play any significant role in placental Lz expansion.
336 Importantly, the effect of IGF2 signalling on feto-placental microvascular remodelling seems
337 specifically driven by fetus-derived IGF2. Accordingly, we did not find any evidence that IGF2 produced
338 by the trophoblast has a direct role on vascularization, being instead required for trophoblast
339 morphogenesis. We therefore suggest that the key role of circulating IGF2 is to provide fetus-derived
340 angiogenic signals to promote the vascular tree expansion in later gestation, in conjunction with local
341 IGF2, derived from the fetal endothelium of the placenta. Mechanistically, likely molecular triggers of
342 fetus-derived IGF2 signalling on microvasculature expansion and trophoblast morphogenesis are
343 IGF2R-ERK1/2-angiopoietin-Tie2/TEK signalling and the key trophoblast differentiation genes *Gcm1*
344 and *Synb*, respectively. Activation of ERK1/2 signalling pathway by IGF2 *via* IGF2R has been observed
345 *in vitro* in previous studies (El-Shewy et al., 2006; El-Shewy et al., 2007). Additionally, primary aortic
346 endothelial cells isolated from *Erk1*/*Erk2* double knockout mice associated transcriptional up-
347 regulation of several DEGs identified in the *Igf2*^{EpiKO} FPECs, including *Angpt2*, *Adamts1*, *Igtp* and *Ifit1*
348 (Srinivasan et al., 2009) (see Figure 5). Although the detailed mechanisms by which ERK1/2 signalling
349 leads to changes in *Angpt2* expression remain to be elucidated, these observations are compatible
350 with a model in which IGF2 binds to IGF2R to activate ERK1/2 signalling pathway, leading to lower
351 *Angpt2* expression, as well as other angiostatic factors (described in Figure 5). We found no evidence
352 for de-regulation of known controllers of placenta angiogenesis, such as VEGF (vascular growth

353 endothelial factor) and PGF (placental growth factor) (Aplin et al., 2020) in these mouse models.
354 Instead, the late gestation angiogenesis defects are related to angiopoietins, although the
355 contribution of other pathways cannot be ruled out. Importantly, angiopoietin-Tie2/TEK signalling has
356 also been implicated in trophoblast morphogenesis, independent of their vascular actions (Kappou et
357 al., 2015), and therefore may be an important link between vascular effects and trophoblast in these
358 models. To our knowledge this is the first report of the impact of the vasculature on trophoblast
359 morphogenesis acting in late gestation.

360 The genetic models used in our study have several limitations. One is the inability to specifically target
361 circulating levels of IGF2 without impacting on the size of the fetus, but also the lack of specific Cre-
362 lines to the placental endothelium. The source of circulating IGF2 is likely to be multi-organ. Unlike for
363 IGF1, the liver is not the main source of circulation IGF2 in mice (Sandovici et al., unpublished).
364 Moreover, and consistent with high expression of IGF2 in mesoderm-derived tissues, deletion of
365 mesodermal *Igf2* enhancers results in reductions in circulating IGF2 by ~50% (Davies et al., 2002).
366 Future transgenic studies targeting specifically circulating IGF2 or placental endothelium are therefore
367 likely to be very challenging. The overexpression IGF2 models (*H19*-DMD^{EpiKO} and *Igf2r*^{ECKO}) used in this
368 study are not without their limitations. Small contributions to the phenotypes due to the actions of
369 the *H19*-encoded *miR-675* and the mannose-6-phosphate receptor roles of IGF2R/activation of TGF-
370 β1 (thus independent of IGF2) cannot be completely ruled out. Indeed, in our study we observed IGF2-
371 independent effects of IGF2R *ex vivo* (reduced basal levels of FPEC proliferation upon siRNA
372 knockdown of *Igf2r*). However, our conclusions that IGF2R is an important IGF2-receptor driving the
373 endothelial cell phenotypes are based on both *in vitro* and *in vivo* evidence. Moreover, *Insr*, and
374 therefore INSR-IGF1R hybrids, are expressed at very low levels in endothelial cells and unlikely to be
375 functional. Endothelial specific deletion of *Igf1r* is not associated with a phenotype. It is important to
376 note that a major target of the *H19*-encoded *mir-675* is IGF1R (Keniry et al., 2012), which is therefore
377 unlikely to be of functional relevance in this context. Importantly, partial redundancy between actions
378 of IGF1R and IGF2R in FPECs cannot be completely ruled out based on this study and warrants future
379 experiments involving dual conditional deletions of *Igf1r* and *Igf2r* driven by *Tek*-Cre.

380 Our study has a number of important implications. It provides insights into the complex interplay
381 between trophoblast branching morphogenesis and placental vascularization. To our knowledge, IGF2
382 is the first example of a fetus-derived hormone-like molecule that signals to the placenta and adapts
383 the expansion of feto-placental microvasculature and trophoblast morphogenesis to the embryo size.
384 Matching placental supply capacity to fetal demand for growth also involves IGF2R – the other
385 imprinted member of the IGF family (Constância et al., 2004). The imprinting of the IGF system is thus
386 likely to have played a key evolutionary role in the origins of the expansion of the feto-placental
387 microvasculature and surface area for nutrient transport throughout pregnancy – a fundamental
388 biological process that is observed in all eutherian species (Fowden et al., 2006). In humans, circulating
389 levels of IGF2 in the umbilical cord progressively increase between 29 weeks of gestation and term,
390 similarly to our findings in the mouse (Gohlke et al., 2004). Additionally, large-for-gestational age and
391 small-for-gestational age babies, have been reported to show increased and reduced levels of IGF2 in
392 the umbilical cord, respectively (Verhaeghe et al., 1993, Tzschoppe et al., 2015). Moreover, placentae
393 obtained from imprinting growth syndrome patients with disrupted IGF2 signalling are often
394 associated with placentomegaly in BWS cases, due to hypervascularization and hyperplasia (Aoki et
395 al., 2011, Armes et al., 2012) and small hypoplastic placentas in SRS cases (Yamazawa et al., 2008),
396 showing striking similarities to our mouse studies. Importantly, most cases of poor placentation in
397 FGR (fetal growth restriction) reported so far were related to placental malperfusion from the
398 maternal side and in response to a perturbed maternal environment (Mayhew et al., 2004). Our

findings suggest that poor placentation in humans could be caused by deficient microvasculature expansion due to reduced fetus-derived IGF2 signalling, with important clinical implications.

ACKNOWLEDGEMENTS

We thank Matt Castle (GSLS Biostatistics Initiative, University of Cambridge) and Wendy Cooper for help with statistical analyses, Jeremy Skepper, Nuala Daw, Barbara Villela and Bliss Anderson for technical assistance with placental stereology and transmission electron microscopy analyses, Adrian Wayman, Laura Hunter (West Forvie Phenomics Center) and Edina Gulacsi (Sferruzzi-Perri laboratory) for help with mouse husbandry; Keli Philips and James Warner (Histology Core Facility) for help with preparing tissue samples for histology and F4/80 staining, Gregory Strachan (Imaging Core Facility) for help with TUNEL$^+$ and F4/80$^+$ cells counting using HALO, Marcella Ma (Genomics and Transcriptomics Core) for help with preparing the RNA-Seq libraries; Evgeniya Shmeleva and Francesco Colucci for advice regarding flow cytometry analyses and providing aliquots of several antibodies used for flow cytometry and FACS; Natalia Savinykh and Esther Perez (NIHR Cambridge BRC Cell Phenotyping Hub) for help with flow cytometry cell sorting. **Funding:** This work was supported by Biotechnology and Biological Sciences Research Council (grant BB/H003312/1 to M.C.), Medical Research Council (MRC_MC_UU_12012/4 to M.C.; MRC_MC_UU_12012/5 to the MRC Metabolic Diseases Unit; MR/R022690/1 to A.N.S-P.), Spanish Ministry of Science and Innovation (RYC-2019-026956 and PID2020-114459RA-I00 to V.P-G.), Royal Society (Dorothy Hodgkin Research Fellowship grant DH130036 to A.N.S-P.), Centre for Trophoblast Research and the NIHR Cambridge BRC Cell Phenotyping Hub.

AUTHOR CONTRIBUTIONS

I.S. and A.G. performed all the *in vivo* experimental work, with contributions from A.H., J.L-T., S.N.S., F.S., K.H. and A.N.S-P. I.S., B.Y.H.L. and G.S.H.Y. performed bioinformatics analyses. I.S., M.R. and C.M.B. performed the *in vitro* tube formation assays. V.P-G. performed the *in vitro Igf2r* knockdown experiments on primary placental endothelial cells. K.B. developed and performed the assay for IGF2 measurements in fetal plasma. I.S. and M.C. designed the project and G.J.B., A.L.F., A.N.S-P. and C.M.B. assisted with the experimental design and data analysis/interpretation. I.S., G.J.B. and M.C. wrote the manuscript, with important contributions from A.L.F., C.M.B. and A.N.S-P. All other authors discussed the results and edited the manuscript. M.C. managed and supervised all aspects of the study.

DECLARATION OF INTERESTS

The authors declare no competing interests.

FIGURE LEGENDS

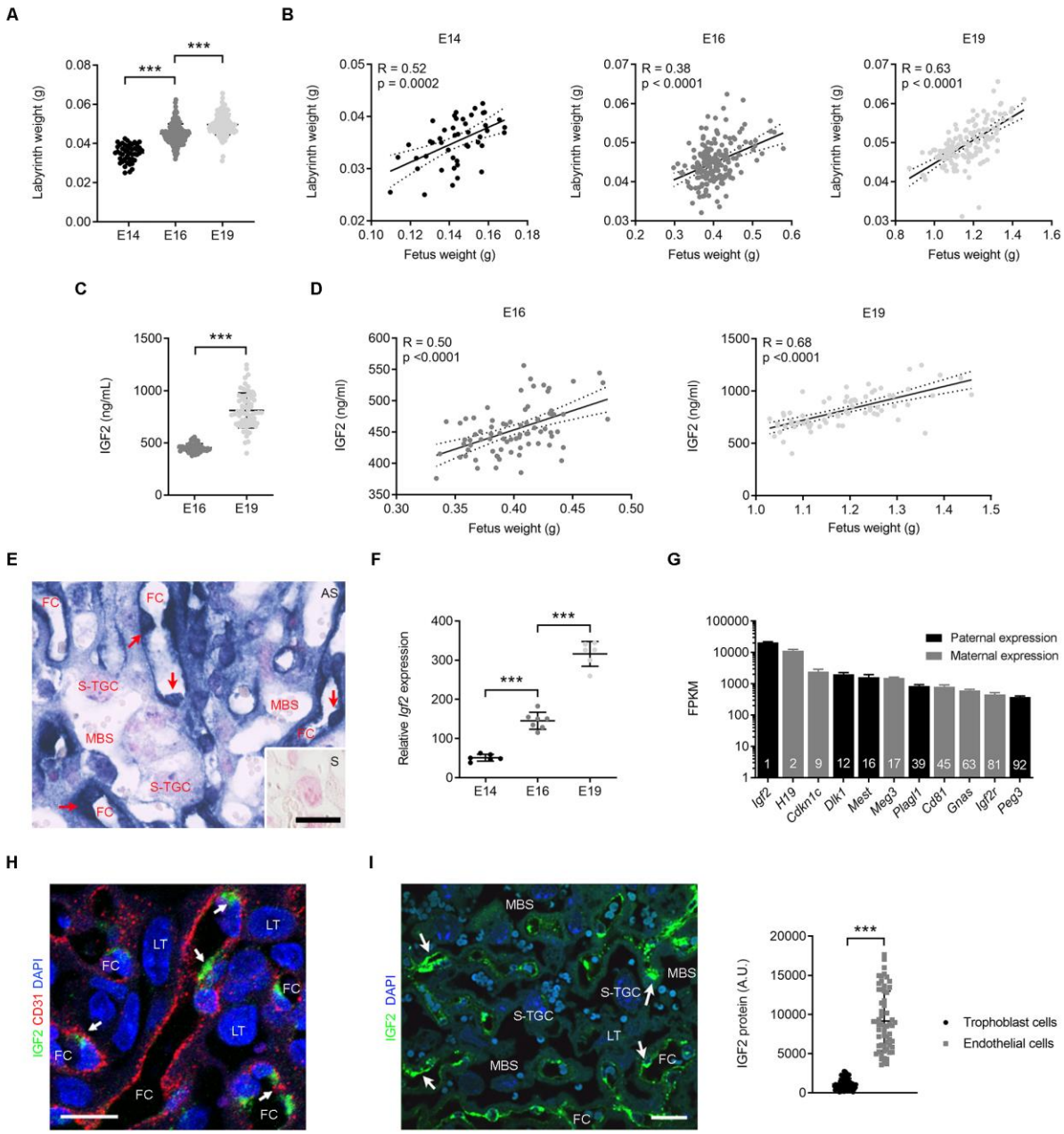

Figure 1. Placental Lz Expansion is Associated with Increasing Levels of Circulating and Endothelial IGF2

(**A**) Weights of micro-dissected labyrinthine zone (Lz). (**B**) Linear correlation analyses between fetal and placental Lz weights [n=46–189 placentae from n>10 litters per group in (A) and (B)]. (**C**) Levels of IGF2 (ng/mL) in plasma of wild-type fetuses. (**D**) Linear correlation analyses between fetal weights and circulating IGF2 [n=70–79 per group in (C) and (D)]. (**E**) *Igf2* mRNA *in situ* hybridization (blue) in E14 wild-type placental Lz (red arrows – FPEC [feto-placental endothelial cells]; AS – antisense probe; inset with sense probe – S; scale bar is 20µm). (**F**) Relative *Igf2* mRNA expression levels measured by qRT-PCR in FPEC from wild-type placental Lz (n=6–7 per group). (**G**) Imprinted genes that rank within top 100 expressed genes in E16 wild-type FPEC (FPKM – Fragments Per Kilobase Million; n=4). (**H**) Double immunostaining for IGF2 and CD31 in E19 wild-type placenta, demonstrating expression of IGF2 in FPEC. Endothelial cells are very thin and hard to detect except where the cytoplasm is more voluminous around the nucleus, with intense IGF2 stain (white arrows). Transmembrane glycoprotein

449 CD31 immunostaining is in the membrane and largely marks endothelial intercellular junctions (scale
450 bar is 20µm)**.** (**I**) Semi-quantitative measurement of IGF2 protein in FPEC versus trophoblast cells (E19
451 wild-type placental Lz, n=60 cells per group from two placentae). White arrows – endothelial cells;
452 scale bar is 50µm. For panels (E), (H) and (I) FC – fetal capillaries; MBS – maternal blood spaces; LT –
453 labyrinthine trophoblast cells; S-TGC – sinusoidal trophoblast giant cells. Data in (A), (C), (F), (G) and
454 (I) is presented as averages ± standard deviation (SD); *** $P<0.001$ calculated by one-way ANOVA plus
455 Tukey's multiple comparisons test in (A) and (F) or by unpaired *t*-test with Welch's correction in (C)
456 and (I). See also Table S1.

457

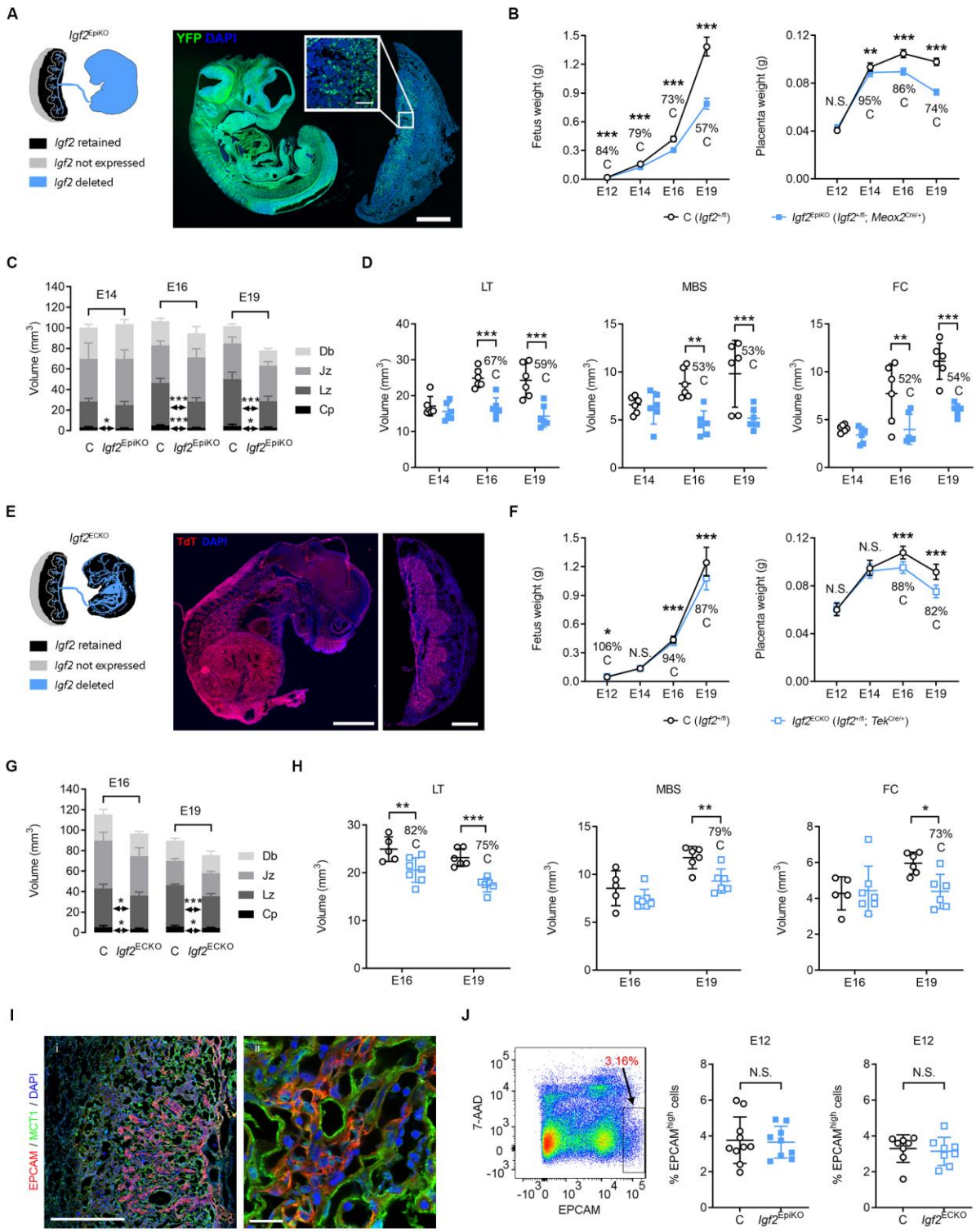

Figure 2. Deletion of *Igf2* in the Epiblast or Endothelium Impairs Placental Lz Expansion

(**A**) Left: schematic of *Igf2* expression in conceptuses with conditional deletion driven by *Meox2*^{Cre}. Right: immunostaining for YFP (green) in a representative fetus and placenta paraffin section at E12 of gestation, double transgenic for *Meox2*^{Cre} and *Rosa26* ^{fl}STOP^{fl}YFP[10] reporter. YFP expression is observed throughout the fetus, and in the placenta is localized to the Lz and chorionic plate (high magnification inset). Blue – DAPI stain for nuclei; scale bars are 1 mm (low magnification) and 100 µm (high magnification). (**B**) Fetal and placental growth kinetics, measured as average wet-weights for

466 each genotype per litter (E12: n=10 litters [n=41 C and n=32 *Igf2*^{EpiKO}]; E14: n=25 litters [n=114 C and
467 n=88 *Igf2*^{EpiKO}]; E16: n=37 litters [n=154 C and n=127 *Igf2*^{EpiKO}]; E19: n=37 litters [n=164 C and n=121
468 *Igf2*^{EpiKO}]). (**C**) Absolute volumes of the placental layers (Db – decidua basalis, Jz – junctional zone, Lz –
469 labyrinthine zone, Cp – chorionic plate), measured by stereology (n=6 per group). (**D**) Absolute
470 volumes (in mm^3) of placental Lz components, measured by stereology (LT – labyrinthine trophoblast,
471 MBS – maternal blood spaces, FC – fetal capillaries) (n=6 per group). (**E**) Left: schematic representation
472 of *Igf2* expression in conceptuses with conditional deletion driven by *Tek*^{Cre}. Right: representative
473 confocal microscopy of frozen sections from a fetus and its corresponding placenta, double transgenic
474 for *TeK*^{Cre} and Ai9(RCL-tdT) reporter at E16 of gestation. Scale bars are 2 mm (fetus) and 1 mm
475 (placenta). (**F**) Fetal and placental growth kinetics (E12: n=5 litters [n=17 C and n=16 *Igf2*^{ECKO}]; E14: n=8
476 litters [n=26 C and n=34 *Igf2*^{ECKO}]; E16: n=13 litters [n=60 C and n=46 *Igf2*^{ECKO}]; E19: n=7 litters [n=31 C
477 and n=27 *Igf2*^{ECKO}]). (**G**) Absolute volumes of the placental layers measured by stereology (n=5–7 per
478 group). (**H**) Absolute volumes (in mm^3) of placental Lz components, measured by stereology (n=5–7
479 per group). (**I**) Double immunostaining for EPCAM (red) and MCT1 (green) in a representative frozen
480 placental section at E12 of gestation. EPCAM expression is observed as clusters of positive cells within
481 the Lz placenta. Blue – DAPI stain for nuclei; scale bars are 500 µm (left panel) and 20 µm (right panel).
482 (**J**) Analysis of EPCAM^{high} positive cells by flow cytometry. Left panel: example of gating used to identify
483 EPCAM^{high} positive cells (the viability dye 7-Aminoactinomycin D [7-AAD] was used to exclude dead
484 cells). Right: quantification of placental EPCAM^{high} positive cells at E12 in conceptuses with conditional
485 *Igf2* deletion driven by *Meox2*^{Cre} (n=10 C and n=9 *Igf2*^{EpiKO} from two litters) or *Tek*^{Cre} (n=8 C and n=8
486 *Igf2*^{ECKO} from two litters). For all graphs data is shown as averages; error bars represent SD in (C), (D),
487 (G), (H) and (J) or 95% confidence intervals (95%CI) in (B) and (F); N.S. – statistically non-significant; *
488 $P<0.05$; ** $P<0.01$; *** $P<0.001$ calculated by a mixed effects model in (B) and (F) (see Materials and
489 Methods), two-way ANOVA plus Sidak's multiple comparisons tests in (D) and (H) or unpaired *t*-tests
490 in (C), (G) and (J). See also Figures S1, S2 and S3.

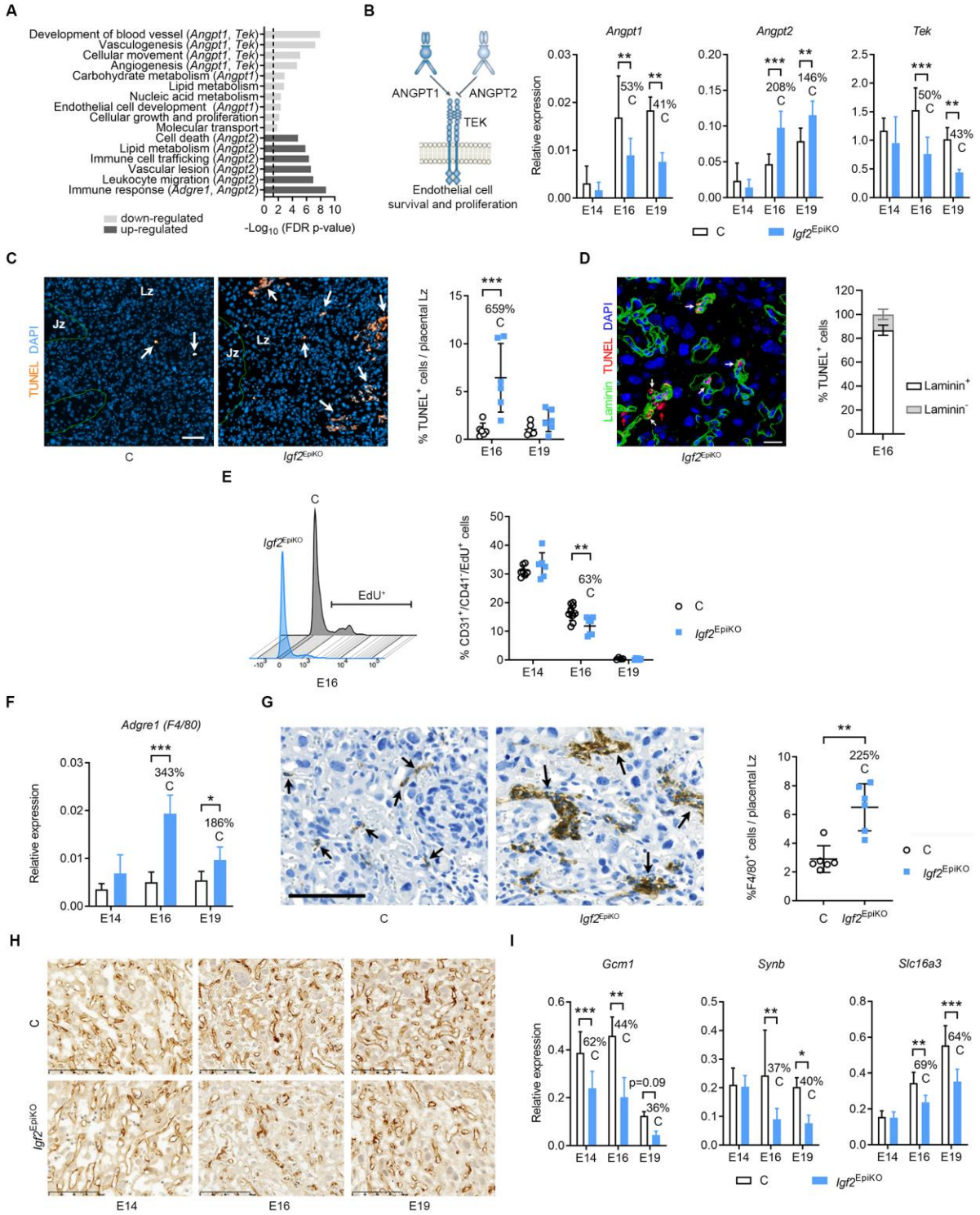

Figure 3. Lack of Fetus-Derived IGF2 Reduces the Expansion of Feto-Placental Microvasculature in Late Gestation

(**A**) Functions enriched in DEGs at E19. (**B**) qRT-PCR analysis of angiopoietin-Tie2/TEK signalling components in placental Lz (n=6–8 per group). (**C**) TUNEL staining in E16 placental Lz (arrows point to apoptotic cells) and data quantification (n=6 samples per group); scale bar is 50µm. (**D**) Left: representative double immunostaining for TUNEL (red) and laminin (green, marker of feto-placental capillaries) in the Lz of an E16 *Igf2*^{EpiKO} mutant placenta (DAPI, blue marks the nuclei; white and red

499 arrows indicate TUNEL^{+} FPECs and LT, respectively; scale bar is 25µm). Right: quantification of TUNEL^{+}
500 cells that are positive or negative for laminin (n=6 *Igf2*^{EpiKO} mutant placentae). (**E**) Feto-placental
501 endothelial cell (FPEC) proliferation measured by flow cytometry (left – representative histograms at
502 E16; right – data quantification; n=4–11 per group). (**F**) qRT-PCR analysis of *Adgre1* in placental Lz. (**G**)
503 Representative F4/80 immunostainings in E16 placental Lz (arrows indicate macrophages). Scale bar
504 is 100µm. Right: percentage of macrophages/placental Lz at E16 (n=6–8 samples per group). (**H**)
505 Representative CD31 immunostaining in placental Lz (scale bar is 100µm). (**I**) qRT-PCR analysis for
506 SynT-II (syncytiotrophoblast layer II) marker genes. For all graphs, data is presented as averages or
507 individual values; error bars are SD; * $P<0.05$, ** $P<0.01$, *** $P<0.001$ by two-way ANOVA plus Sidak's
508 multiple comparisons tests in (B), (C), (E), (F) and (I) or Mann-Whitney tests in (G). See also Figure S4
509 and Table S2.

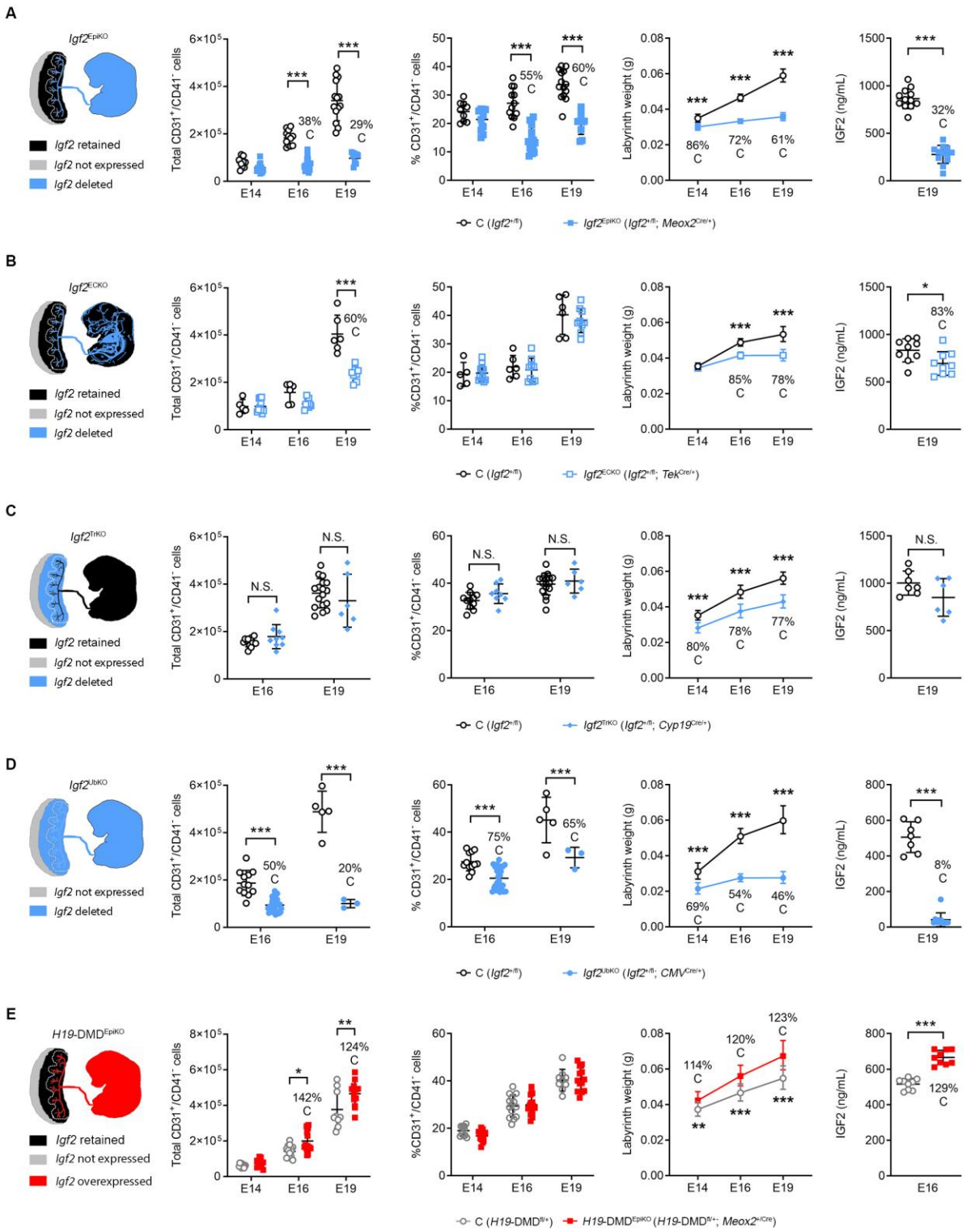

Figure 4. Genetic Models of Mismatched Placental and Fetal Growth Reveal Circulating IGF2 as a Major Endocrine Regulator of FPEC and Placental Lz Expansion

Column 1: schematic diagrams of the genetic models: *Igf2*^{EpiKO} (**A**), *Igf2*^{ECKO} (**B**), *Igf2*^{TrKO} (**C**), *Igf2*^{UbKO} (**D**) *H19*-DMD^{EpiKO} (**E**). Columns 2 and 3: total numbers (column 2) and proportion of FPEC/placental Lz (column 3), measured by flow cytometry (n conceptuses per group: *Igf2*^{EpiKO}: n=9–18; *Igf2*^{ECKO}: n=5–11; *Igf2*^{TrKO}: n=6–17; *Igf2*^{UbKO}: n=3–26; *H19*-DMD^{EpiKO}: n=9–15). Column 4: placental Lz growth kinetics (*Igf2*^{EpiKO}: n=9–20 litters; *Igf2*^{ECKO}: n=3–9 litters; *Igf2*^{TrKO}: n=4–9 litters; *Igf2*^{UbKO}: n=3–8 litters; *H19*-

518 DMD^{EpiKO}: n=3–4 litters). Column 5: IGF2 levels (ng/mL) in plasma (n per group: *Igf2*^{EpiKO}: n=12; *Igf2*^{ECKO}:
519 n=9; *Igf2*^{TrKO}: n=6–7; *Igf2*^{UbKO}: n=7–11; *H19*-DMD^{EpiKO}: n=9). Data is shown as averages or individual
520 values and error bars are SD (columns 2, 3 and 5) and 95% CI (column 4). N.S. – not significant; *
521 *P*<0.05; ** *P*<0.01; *** *P*<0.001 calculated by two-way ANOVA plus Sidak's multiple comparisons tests
522 (second and third columns), mixed effects model (fourth column) or Mann Whitney tests (fifth
523 column). See also Figures S5A, S5B and S6.

524

525

526

527

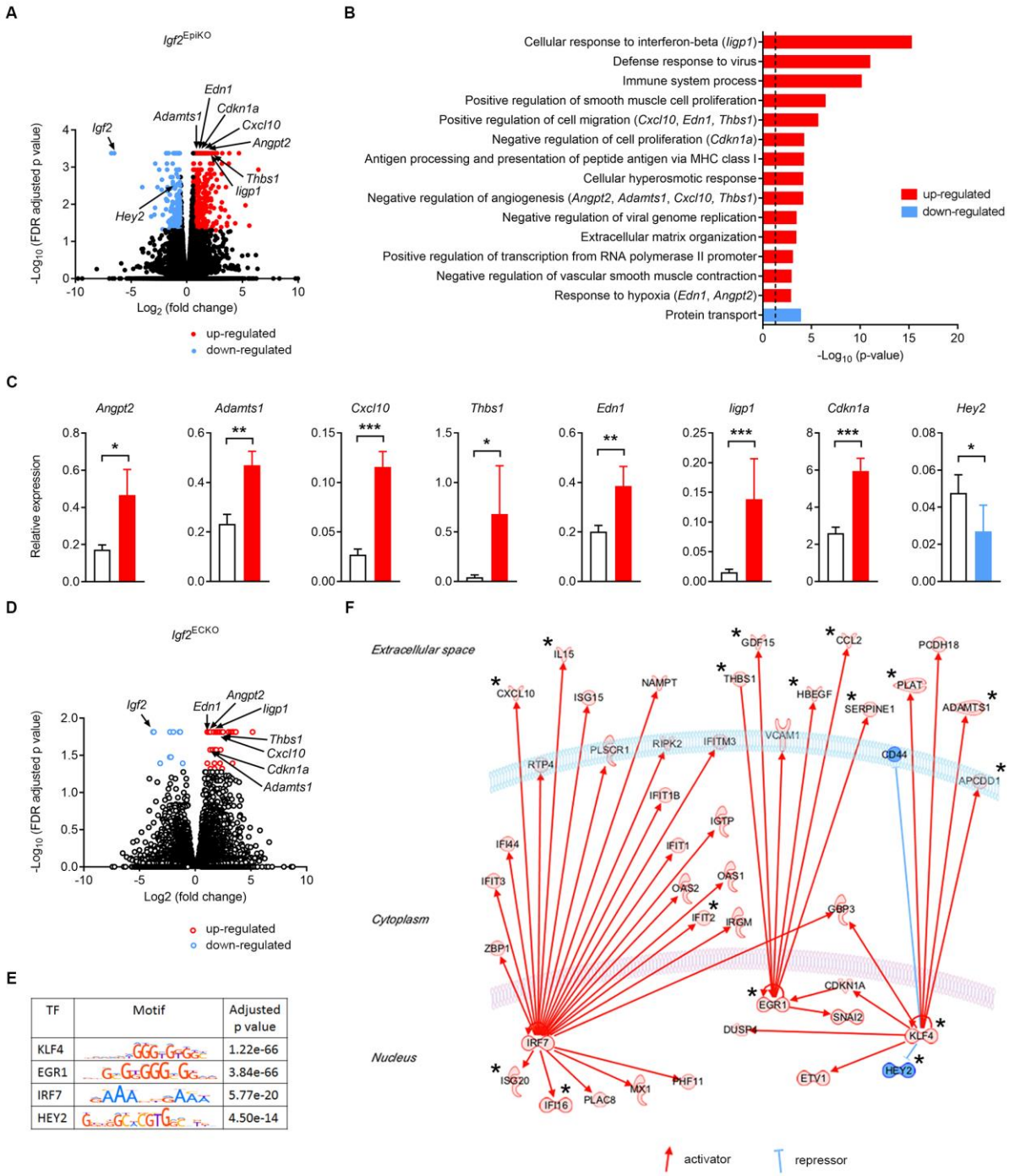

528

529 **Figure 5. IGF2 Signalling Regulates Angiogenic Properties of Endothelial Cells**

530 (**A**) Volcano plot representation of differentially expressed genes (DEGs) identified by RNA-seq in E16
531 FPEC (*Igf2*^{EpiKO} versus controls). Significant up-regulated and down-regulated DEGs (FDR<0.05) are
532 shown with red and blue, respectively. (**B**) Top scoring biological processes enriched in DEGs.
533 Biologically validated DEGS are listed in parentheses. The dotted line corresponds to FDR-corrected *P*
534 value of 0.05. (**C**) Biological validation. Data is shown as averages (n=11-12 samples per group); error
535 bars are SEM; * *P*<0.05, ** *P*<0.01, *** *P*<0.001 calculated by Mann-Whitney tests. (**D**) Volcano plot
536 representation of DEGs identified by RNA-seq in E16 FPEC (*Igf2*^{ECKO} versus controls). Significant up-
537 regulated and down-regulated DEGs (FDR<0.05) are shown with red and blue, respectively. (**E**)
538 Transcription factors (TFs) identified by Analysis of Motif Enrichment (AME). (**F**) IPA regulatory

network built with the four TFs identified using AME analysis. Proteins labelled with * are known regulators of angiogenesis (angiostatic or pro-angiogenic factors) and key references are listed in Table S4. See also Figures S5C and S5D and Table S3.

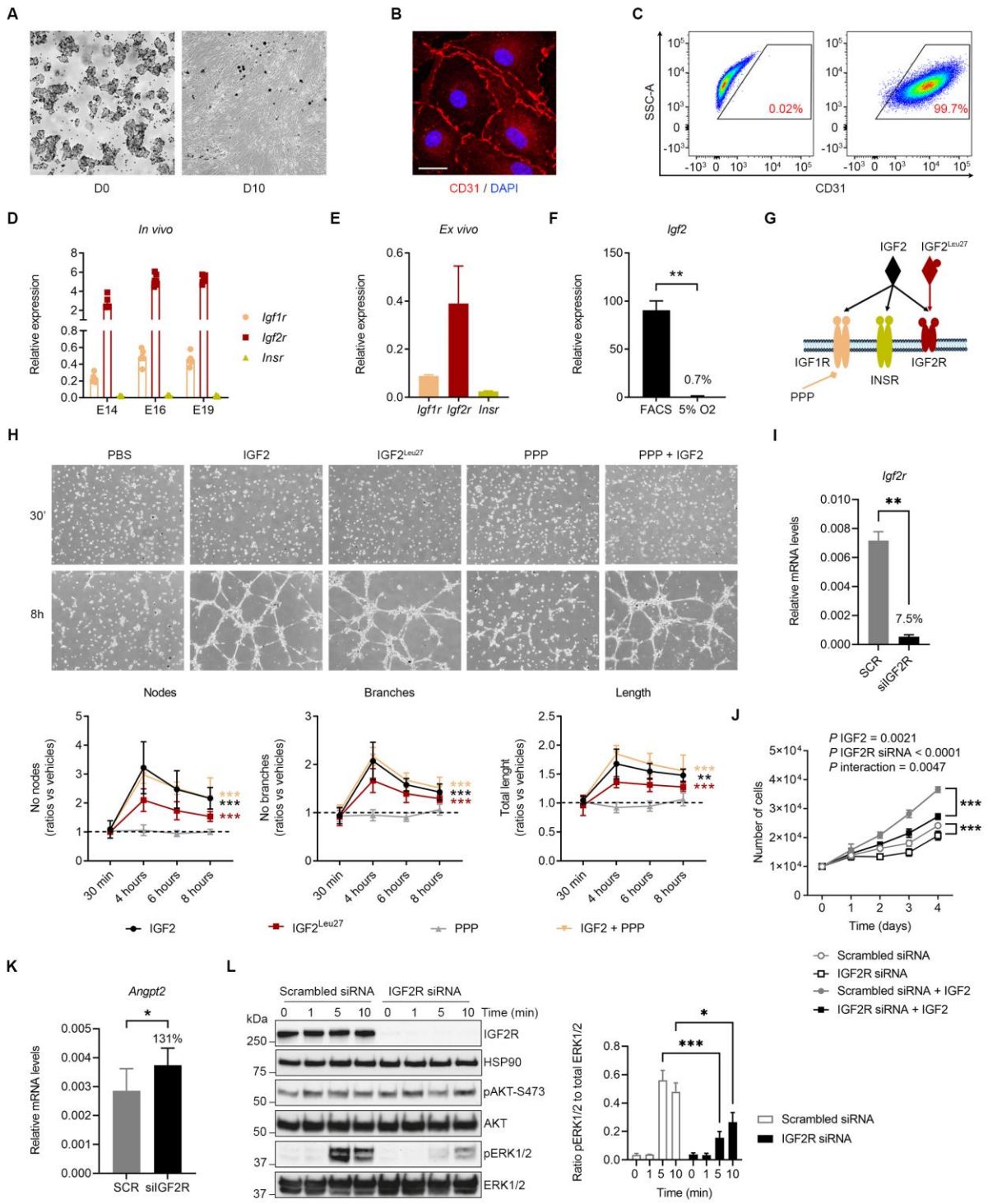

547

548 **Figure 6. IGF2 Acts on Feto-Placental Endothelial Cells *via* IGF2R-ERK signalling *ex vivo***

549 (**A**) Primary feto-placental endothelial cell (FPEC) isolated from E16 placental Lz: D0 – freshly isolated
550 cells, bound to magnetic beads coated with anti-CD31 antibodies; D10 – FPEC at passage one (after
551 approximately 10 days of culture). (**B**) Confocal imaging of passage one FPEC, stained for CD31 (scale
552 bar is 20 µm). (**C**) Flow cytometry analysis of passage one FPEC stained for CD31, demonstrating that
553 these are almost exclusively CD31^{+}. (**D**) qRT-PCR analysis for *Igf1r*, *Igf2r* and *Insr* in FPECs isolated by
554 FACS (n=6–7 per group). (**E**) Relative expression of the three IGF receptors in passage one FPEC. (**F**)
555 qRT-PCR analysis of *Igf2* mRNA levels in passage one FPEC cultured in 5% O2 versus primary FPEC

556 isolated from E16 placental Lz by FACS. (**G**) Schematic representation of IGF2 and IGF receptors.
557 IGF2^{Leu27} analogue acts specifically on IGF2R and picropodophyllin (PPP) inhibits phosphorylation of
558 IGF1R. (**H**) Representative images of capillary-like tube formation assay in primary FPEC seeded on
559 matrigel and exposed to exogenous IGF2, IGF2^{Leu27}, PPP or PPP+IGF2 (equal seeding of cell numbers at
560 30 min and tube formation at 8 hours), and quantification of number of nodes, branches and total
561 length (n=5–6 independent experiments). (**I**) qRT-PCR analysis of *Igf2r* mRNA levels in primary FPECs
562 upon knockdown by siRNA (n=8 samples/group). (**J**) Proliferation assay of primary FPEC with or
563 without IGF2R siRNA knockdown, in presence or absence of IGF2, on 4 consecutive days after plating.
564 Cells with IGF2R siRNA knockdown exhibit significant proliferation defects that are further
565 accentuated upon IGF2 treatment (n=5 biological replicates per group). (**K**) qRT-PCR analysis of *Angpt2*
566 mRNA levels in primary FPECs transfected with scrambled siRNA or IGF2R siRNA, upon 4 days of
567 treatment with 50 ng/mL mouse recombinant IGF2 (n=8 samples/group). (**L**) Left side: identification
568 of delayed ERK1/2 phosphorylation in FPECs with IGF2R siRNA knockdown upon acute treatment with
569 50ng/mL mouse recombinant IGF2. HSP90 was used as internal control for protein loading. Right side:
570 quantification of ratios pERK1/2 to total ERK1/2 for n=3 independent biological replicates. For all
571 graphs, data is presented as averages or individual values and error bars represent SEM. * $P<0.05$, **
572 $P<0.01$ and *** $P<0.001$ calculated by a Mann Whitney test in (F), two-way ANOVA tests with Sidak's
573 multiple comparisons test in (H), (J) and (L), Wilcoxon matched-pairs signed rank test in (I) and paired
574 student *t*-test in (K).

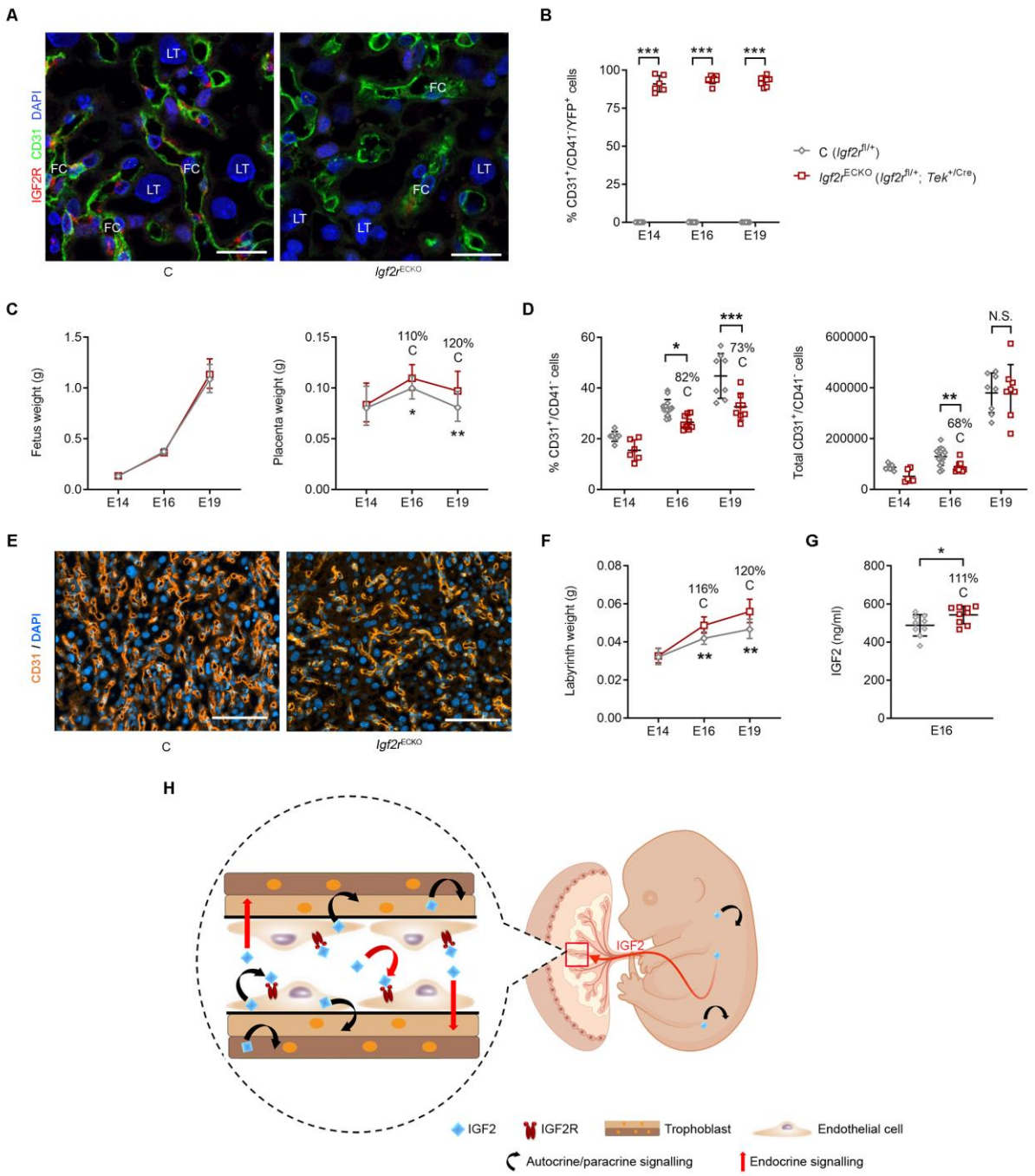

Figure 7. IGF2 Acts on Feto-Placental Endothelial Cells via IGF2R *in vivo*

(**A**) Representative double immunostaining for IGF2R (red) and the endothelial cell marker CD31 (green) in *Igf2r*^{ECKO} mutant and control placental Lz at E16 (DAPI, blue marks the nuclei; FC – fetal capillaries, LT – labyrinthine trophoblast; scale bar is 25µm). (**B**) Flow cytometry analysis showing that the majority (>80%) of *Igf2r*^{ECKO} mutant feto-placental endothelial cells (FPECs) express YFP, demonstrating good efficiency of *Tek2*^{Cre} in these samples (n=6–14 per genotype). (**C**) Fetal and placental growth kinetics in *Igf2r*^{ECKO} (*Igf2r*$^{fl/+}$; *Tek*$^{+/Cre}$) mutants compared to *Igf2r*$^{fl/+}$ controls (n=8–28 conceptuses from n=3-8 litters for each developmental stage). (**D**) Proportion and total numbers of FPEC/placental Lz measured by flow cytometry (n=6–14 per group). (**E**) Representative CD31 immunofluorescence staining in E16 placental Lz (scale bar is 100µm). (**F**) Placental Lz growth kinetics: *Igf2r*^{ECKO} (n=8–16 conceptuses per group). (**G**) IGF2 levels (ng/mL) in plasma at E16 (n=9 per group).

587 (**H**) Model summarizing the proposed actions of fetus-, endothelial- and trophoblast-derived IGF2. For
588 all graphs, data is presented as averages or individual values and error bars represent SD in (B), (D),
589 and (G), or 95%CI in (C) and (F). N.S. – not significant; * $P<0.05$; ** $P<0.01$; *** $P<0.001$ calculated by
590 two-way ANOVA tests in (B), and (D), mixed effects model in (C) and (F) and Mann Whitney tests in
591 (G). See also Figure S7.

592

593 **STAR*METHODS**

594 **Key Resources Table**

REAGENT or RESOURCE	SOURCE	IDENTIFIER
Experimental models: organisms/strains		
Mouse *Igf2*$^{fl/fl}$	Hammerle et al., 2020	n/a
Mouse *Meox2*^{Cre}	Tallquist et al., 2000	The Jackson Laboratory (Stock No: 003755)
Mouse *Tek*^{Cre}	Kisanuki et al., 2001	The Jackson Laboratory (Stock No: 008863)
Mouse *Cyp19*^{Cre}	Wenzel and Leone, 2007	n/a
Mouse *CMV*^{Cre}	Schwenk et al., 1995	The Jackson Laboratory (Stock No: 006054)
Mouse *Vav*^{iCre}	de Boer et al., 2003	The Jackson Laboratory (Stock No: 008610)
Mouse *Rosa26* ^{fl}STOP^{fl}YFP	Srinivas et al., 2001	The Jackson Laboratory (Stock No: 006148)
Mouse Ai9(RCL-tdT)	Madisen et al., 2010	The Jackson Laboratory (Stock No: 007909)
Mouse *H19*-DMD$^{fl/fl}$	Srivastava et al., 2000	n/a
Mouse *Igf1r*$^{fl/fl}$	Dietrich et al., 2000	The Jackson Laboratory (Stock No: 012251)
Mouse *Igf2r*$^{fl/fl}$	Wylie et al., 2003	n/a
Mouse: C57BL/6J	Charles River	n/a
Antibodies		
rat anti-mouse IGF-II	R&D Systems	840962
biotinylated goat anti-mouse IGF-II	R&D Systems	840963
anti-DIG-AP antibody	Roche	11093274910
goat anti-human IGF2	R&D Systems	AF292
goat anti-mouse SOD1	R&D Systems	AF3787
rabbit anti-goat IgG-HRP	Santa Cruz	sc-2768
goat anti-GFP	Abcam	ab6673
rabbit anti-CD31	Abcam	ab28364
goat anti-CD31	R&D Systems	AF3628
rat anti-mouse F4/80	R&D Systems	MCA497
chicken anti-MCT1	Merk Millipore	AB1286-I
rabbit anti-MCT4	Merk Millipore	AB3314P
rabbit anti-laminin	Dako	Z0097
rabbit anti-pan cytokeratin	Novus Biologicals	nb600-579

rat anti-mouse CD326/Epcam	BD Biosciences	552370
donkey anti-goat-AF488	Jackson ImmunoResearch	705-546-147
donkey anti-rabbit-AF594	Jackson ImmunoResearch	711-546-152
goat anti-rabbit, biotinylated	Abcam	ab6720
NL557-conjugated donkey anti-goat	R&D Systems	NL001
rabbit anti-rat	Bethyl	A110-322A
anti-rabbit HRP	Vector Labs	MP-7451
donkey anti-chicken-AF488	Jackson ImmunoResearch	703-546-155
goat anti-rabbit-AP	Abcam	ab6722
donkey anti-rat-AF594	Thermo Fisher Scientific	A-21209
rat anti-CD16/32	BioLegend	101320
rat anti-mouse CD41-PE	BioLegend	133906
rat anti-mouse CD31-AF647	BioLegend	102516
rat anti-mouse CD326-AF647	BioLegend	118212
rat anti-mouse CD41-BV421	BioLegend	133911
rat anti-mouse CD117-PE	BioLegend	105808
rat anti-mouse Ly-6A/E-BV510	BioLegend	108129
rat anti-lineage cocktail-BV421	BioLegend	133311
and rat anti-mouse CD45-V500	BD Horizon	561487
rat anti-mouse CD34-AF700	Thermo Fisher Scientific	56-0341-82
rabbit anti IGF2R	Cell Signaling	14364
mouse anti-Phospho-p44/42 MAPK (Erk1/2) (Thr202/Tyr204)	Cell Signaling	9106
rabbit anti-p44/42 MAPK (Erk1/2)	Cell Signaling	9102
rabbit anti-Phospho-Akt (Ser473)	Cell Signaling	9271
rabbit anti-Akt	Cell Signaling	9272
rabbit anti-HSP90	Cell Signaling	4877
Chemicals/reagents		
Mouse IGF-II DuoSet ELISA kit	R&D Systems	DY792
RIPA buffer	Sigma	R0278
Streptavidin Sulpho-TAG	MSD	R32AD-1
biotinylated lectin	Vector Laboratories	B-1205
pCR2.1-TOPO plasmid	Thermo Fisher Scientific	K450002
Digoxigenin	Roche	11175025910
blocking reagent	Roche	1096176001

BCIP/NBT mix	Promega	S3771
Pierce BCA Assay Protein kit	Thermo Fisher Scientific	23225
12-well NuPAGE Novex 4-12% Bis-Tris precast gels	Thermo Fisher Scientific	NP0322BOX
Novex Sharp protein standard	Invitrogen	LC5800
iBlot Transfer Stacks	Invitrogen	IB3010-01
Clarity ECL Western Blotting Substrate	Bio-Rad	1705060
stripping buffer	Thermo Fisher Scientific	21059
In Situ Cell Death Detection Kit, TMR red	Sigma	012156792910
TUNEL Assay Kit – BrdU-Red	Abcam	ab66110
Click-iT EdU Alexa Fluor 488 Imaging Kit	Invitrogen	C10337
DAPI	Sigma	D9542
RNeasy Plus Micro Kit	Qiagen	74034
RNeasy Plus Mini Kit	Qiagen	74134
RNeasy Midi Kits	Qiagen	75144
RNA 6000 Pico Kit	Agilent	5067-1513
RNA 6000 Nano Kit	Agilent	5067-1511
RevertAid RT Reverse Transcription Kit	Thermo Fisher Scientific	K1622
SYBR Green JumpStart Taq Ready Mix	Sigma	S4438
Mouse Gene 1.0 ST Array	Affymetrix	901171
RBC lysis buffer	BioLegend	420301
staining buffer	BioLegend	420201
7-Aminoactinomycin	Invitrogen	A1310
5-ethynyl-2'-deoxyuridine	Thermo Fisher Scientific	A10044
Red LIVE/DEAD Fixable Dead Cell Stain	Thermo Fisher Scientific	L23102
Click-iT EdU Alexa Fluor 488 Flow Cytometry Assay Kit	Thermo Fisher Scientific	C10420
collagenase type I	Sigma	SCR103
endothelial mitogens	Sigma	E2759
serum replacement media	Sigma	S0638
mouse recombinant IGF2	R&D Systems	792-MG-050
human $IGF2^{Leu27}$	GroPep	TU100
picropodophyllotoxin	Sigma	T9576
Accutase	Sigma	A6964
Angiogenesis µ-Slides	Ibidi	81506
matrigel	BD Biosciences	354234
primary placental microvascular	Cell Biologics	C57-6056

endothelial cells isolated from C57BL/6J mice		
complete endothelial growth medium	Cell Biologics	M1168
basal endothelial growth medium	Cell Biologics	M1168b
stealth siRNA for *Igf2r*	Thermo Fisher Scientific	1320003
stealth scrambled siRNA	Thermo Fisher Scientific	12935100
Lipofectamine RNAiMax transfection reagent	Thermo Fisher Scientific	13778075
protease inhibitor cocktail	Sigma	P2714
enhanced chemiluminescence reaction	GE Healthcare	RPN2209
streptavidin-horse radish peroxidase	Rockland	S000-03
DAB	Dako	K3468
DAB	Sigma	D3939
ImmPact DAB kit	Vector Labs	SK-4105
NBT/BCIP containing levimasole	Thermo Fisher Scientific	34070
Oligonucleotides		
Igf2$^{fl/fl}$-F	TTACAGTTCAAAGCCACCACG	This study
Igf2$^{fl/fl}$-RW	GCCAAAGAGATGAGAAGCACC	This study
Igf2$^{fl/fl}$-RD	GCCAAACACAGTAAAAAGAAATGC	This study
Rosa26^{fl}*STOP*^{fl}*YFP*-F	TGTTATCAGTAAGGGAGCT	This study
Rosa26^{fl}*STOP*^{fl}*YFP*-R-WT	CACACCAGGTTAGCCTTTA	This study
Rosa26^{fl}*STOP*^{fl}*YFP*-R-fl	AAGACCGCGAAGAGTTTGT	This study
Meox2-Cre-F	GGACCACCTTCTTTTGGCTTC	This study
Meox2-Cre-R-WT	AAGATGTGGAGAGTACGGGGTAG	This study
Meox2-Cre-R-Cre	CAGATCCTCCTCAGAAATCAGC	This study
Tek-Cre-F	TGTAAACAAGAGCGAGTGGA	This study
Tek-Cre-R-WT	AGAGAATGGCGAGAAGTCAC	This study
Tek-Cre-R-Cre	TGAGTGAACGAACCTGGTCG	This study
Vav-iCre-F-WT	ATGTCTCCAATCCTTGAACACTG	This study
Vav-iCre-R-WT	GCAGTGGGAGAAATCAGAACC	This study
Vav-iCre-F-Vav	GACTACCTCCTGTACCTGCAAG	This study
Vav-iCre-R-Vav	ACTCTGATTCTGGCAATTTCGG	This study
Cyp19-Cre-F	GACCTTGCTGAGATTAGATC	This study
Cyp19-Cre-R	AGAGAGAAGCATGTTTAGCTGG	This study
CMV-Cre-F	CGAGTGATGAGGTTCGCAAG	This study
CMV-Cre-R	TGAGTGAACGAACCTGGTCG	This study
H19-DMD$^{fl/fl}$-F	CAGGCCTGTCCTCACCTGAAC	This study
H19-DMD$^{fl/fl}$-R	GCCAGCTTGCCTTGGCAACCCCTT	This study
Igf2r$^{fl/fl}$-F	CCTTCCCTCCAGGCCGTTAC	This study
Igf2r$^{fl/fl}$-R	GGTGAGGTCTCCATCTGAGTACC	This study
Igf1r$^{fl/fl}$-F	CTTCCCAGCTTGCTACTCTAGG	This study
Igf1r$^{fl/fl}$-R	CAGGCTTGCAATGAGACATGGG	This study
qRT-*Igf2*-F	AGTCCGAGAGGGACGTGTCTA	This study

qRT-*Igf2*-R	CGGACTGTCTCCAGGTGTCAT	This study
qRT-*Angpt1*-F	GAAGCAACTTCTCAACAGACA	This study
qRT-*Angpt1*-R	TTCTTTGTGTTTTCCCTCCATT	This study
qRT-*Angpt2*-F	CTTCTACCTCGCTGGTGAAGAG	This study
qRT-*Angpt2*-R	GCTAAAATCACTTCCTGGTTGG	This study
qRT-*Tek*-F	GGAGTGGAGTGAAGAACTAGG	This study
qRT-*Tek*-R	GTGGAGTCAGTGATGTTGGAGA	This study
qRT-*Fas*-F	CTGCAGACATGCTGTGGATCT	This study
qRT-*Fas*-R	GCCTCCTCAGCTTTAAACTCTC	This study
qRT-*Ctss*-F	AGAGACCCTACCCTGGACTACC	This study
qRT-*Ctss*-R	GATTCTTTTCCCAGATGAGACG	This study
qRT-*Spp1*-F	ACCATGAGATTGGCAGTGATTT	This study
qRT-*Spp1*-R	GAGCTGCCAGAATCAGTCACTT	This study
qRT-*Tnnc1*-F	GATCTCTTCCGCATGTTTGAC	This study
qRT-*Tnnc1*-R	TCAATGTCATCTTCCGTAATGG	This study
qRT-*Myocd*-F	ATTCCTGTGCACACTGCTGTAA	This study
qRT-*Myocd*-R	GAGCTTCTTCACCTTTGGTTTG	This study
qRT-*Apobec1*-F	GCACACCTGAGGAAACAAAGTC	This study
qRT-*Apobec1*-R	CAGAGTGGGATCAACAGCTACA	This study
qRT-*Cd72*-F	CCAAGGAGAACCTGAAAACTGA	This study
qRT-*Cd72*-R	GCACCTTTCCTGATATGGAATC	This study
qRT-*Dusp14*-F	CTCCCTGGAAATCCTTAGCAC	This study
qRT-*Dusp14*-R	ACCTCTGGAGCTCATGAAGATG	This study
qRT-*Bmp10*-F	CTCTACAACAAATTCGCCACAG	This study
qRT-*Bmp10*-R	GAGCCCATTAAAAGTGACTGGT	This study
qRT-*Igfbp3*-F	CAGGCAGCCTAAGCACCTAC	This study
qRT-*Igfbp3*-R	GGAACTTGGAATCGGTCACTC	This study
qRT-*Adgre1*-F	TAGCTGCTCTTCTGATACCCTC	This study
qRT-*Adgre1*-R	CCAACATTCATCTTGTCCCCTC	This study
qRT-*Gcm1*-F	CCGCAAGATTTACCTGAGACC	This study
qRT-*Gcm1*-R	GAATAAGCTTCAGGGGTCCATT	This study
qRT-*Syna*-F	AGCCCTCTCTGGACAATATTCA	This study
qRT-*Syna*-R	CAAGGTGGGAGAAGATATTTGG	This study
qRT-*Synb*-F	CAGCTGACACCCTCATTAAACA	This study
qRT-*Synb*-R	ATCCAGAAATGGGAATGAAGTG	This study
qRT-*Slc16a1*-F	TCGCAGCTTCTTTCTGTAACAC	This study
qRT-*Slc16a1*-R	TCATAGTCAGAGCTGGGTTCAA	This study
qRT-*Slc16a3*-F	TGCAGAAGCATTATCCAGATCTAC	This study
qRT-*Slc16a3*-R	GTATCGATTGAGCATGATGAGG	This study
qRT-*Ly6e*-F	ACATGAGAGTCTTCCTGCCTGT	This study
qRT-*Ly6e*-R	TTCTGATCGGTACATGAGAAGC	This study
qRT-*Adamts1*-F	CAAAGGACAGGTGCAAGCTC	This study
qRT-*Adamts1*-R	TTGCACACAGACAGAGGTAGAG	This study
qRT-*Cxcl10*-F	CGTCATTTTCTGCCTCATCCTG	This study
qRT-*Cxcl10*-R	TGATTTCAAGCTTCCCTATGGC	This study
qRT-*Thbs1*-F	ATGTACCCATCCAGAGCATCTT	This study
qRT-*Thbs1*-R	GGTTCCAAAGACAAACCTCACA	This study
qRT-*Edn1*-F	GACATCATCTGGGTCAACACTC	This study
qRT-*Edn1*-R	AAGTCTTTCAAGGAACGCTTGG	This study
qRT-*Iigp1*-F	ATGATTTGCCCTCCAGCTTTAC	This study

qRT-*Iigp1*-R	ACTGAATATTCCCTTTTCTCATCCT	This study
qRT-*Cdkn1a*-F	GAACATCTCAGGGCCGAAAAC	This study
qRT-*Cdkn1a*-R	CACTTCAGGGTTTTCTCTTGCA	This study
qRT-*Hey2*-F	CTGCCAAGTTAGAAAAGGCTGA	This study
qRT-*Hey2*-R	CTCATGAAGTCTGTGGCAAGAG	This study
qRT-*Igf1r*-F	GTTATCCACGACGATGAGTGC	This study
qRT-*Igf1r*-R	AGTCACCGAATCGATGGTTTTC	This study
qRT-*Igf2r*-F	GGAAGACACCAGAACCAGACA	This study
qRT-*Igf2r*-R	TGACACTCATCCTCTGGAAGC	This study
qRT-*Insr*-F	GAGAGGATGTGAGACGACGG	This study
qRT-*Insr*-R	AGCAGTTCTCCAGCTCATGTAG	This study
qRT-*Gapdh*-F	ACAACTCACTCAAGATTGTCAGCA	This study
qRT-*Gapdh*-R	ATGGCATGGACTGTGGTCAT	This study
qRT-*Sdha*-F	TTCCGTGTGGGGAGTGTATTG	This study
qRT-*Sdha*-R	ATTCTGCAGCTCCAGGGTCTC	This study
qRT-*Pmm1*-F	ATCCGGGAGAAGTTTGTGGAA	This study
qRT-*Pmm1*-R	GCTGTCTTCATCCAGGCTGTC	This study
qRT-*Ppia*-F	AAGGGTTCCTCCTTTCACAGAA	This study
qRT-*Ppia*-R	GATGCCAGGACCTGTATGCTT	This study
Software and algorithms		
GraphPad Prism 8 software	GraphPad	https://www.graphpad.com/
R3.3	R Foundation	https://www.r-project.org/
MSD Workbench Software	MSD	https://www.mesoscale.com
ImageLab	Bio-Rad	https://www.bio-rad.com
NewCAST	Visiopharm	https://visiopharm.com
ZEN 2009	Carl Zeiss	https://www.zeiss.com/microscopy
Volocity 6.3	Improvision	https://www.perkinelmer.com
HALO	PerkinElmer	https://www.perkinelmer.com
GeneSpring GX 12.1	Agilent	https://www.agilent.com
Ingenuity Pathway Analysis	Qiagen	https://digitalinsights.qiagen.com
FlowJo v.10	TreeStar	https://www.flowjo.com
Angiogenesis Analyzer	Schneider et al., 2012	https://imagej.nih.gov/ij/
TopHat 2.0.11	Kim et al., 2013	https://ccb.jhu.edu/software/tophat
Cufflinks 2.2.1	Trapnell et al., 2010	https://github.com/cole-trapnell-lab/cufflinks
DAVID v6.8	LHRI	https://david.ncifcrf.gov/
REViGO	Supek et al., 2011	http://revigo.irb.hr
EPD	Swiss Institute of Bioinformatics	https://epd.vital-it.ch/index.php
AME v4.12.0	MEME Suite	http://meme-suite.org

RESOURCES AVAILABILITY

Lead contact

598 Further information and requests for resources and reagents should be directed to and will be fulfilled
599 by the Lead Contact, Miguel Constância (jmasmc2@cam.ac.uk).

600 **Materials availability**

601 This study did not generate new unique reagents.

602 **Data and code availability**

603 Processed gene expression data from expression microarray and RNA-seq comparisons are available
604 in Tables S1–S3 and the corresponding raw data have been deposited in the Gene Expression Omnibus
605 (GEO) under the accession numbers GSE125434 and GSE179549. Other data and materials are
606 available upon request from the corresponding authors.

607 **EXPERIMENTAL MODEL AND SUBJECT DETAILS**

608 **Mice**

609 Mice were bred, maintained and mated under pathogen-free conditions at the University of
610 Cambridge Phenomics Unit (West Forvie), in accordance with the University of Cambridge Animal
611 Welfare and Ethical Review Body and the United Kingdom Home Office Regulations. The morning of
612 the copulation plug discovery was counted as embryonic day 1 (E1).

613 The *Igf2*$^{fl/fl}$ mice were generated in our laboratory (Hammerle et al., 2020). *Meox2*^{Cre} mice (Tallquist et
614 al., 2000), *Tek*^{Cre} mice (Kisanuki et al., 2001), *CMV*^{Cre} mice (Schwenk et al., 1995) and *Igf1r*$^{fl/fl}$ mice
615 (Dietrich et al., 2000) were imported from the Jackson Laboratory (Maine, USA). *Meox2*^{Cre} is active
616 starting at E5 in the epiblast, which gives rise to the entire embryo proper and FPEC (Tallquist et al.,
617 2000). *Tek*^{Cre} (also known as *Tie2*^{Cre}) activity starts at E7.5 in the endothelial cell lineage, including FPEC
618 (Kisanuki et al., 2001). *CMV*^{Cre} activity starts soon after fertilization and induces ubiquitous deletion of
619 floxed alleles in all tissues, including the germline (Schwenk et al., 1995). *Cyp19*^{Cre} mice (Wenzel and
620 Leone, 2007) were kindly provided by Prof. Gustavo Leone (Medical University of South Carolina).
621 *Cyp19*^{Cre} is active from E6.5 in the early diploid trophoblast cells that give rise to spongiotrophoblast,
622 giant cells, and labyrinthine trophoblast cells (Wenzel and Leone, 2007). *Vav*^{iCre} mice, in which
623 expression of an optimized variant of Cre is expressed in all hematopoietic cells but not in endothelial
624 cells (de Boer et al., 2003), were kindly provided by Dr. Bidesh Mahata (University of Cambridge).
625 (*Rosa26* ^{fl}STOP^{fl}YFP mice (Srinivas et al., 2001) were kindly provided by Dr. Martin Turner (The
626 Babraham Institute, Cambridge), Ai9(RCL-tdT) mice (Madisen et al., 2010) by Prof. William Colledge
627 (University of Cambridge), *H19*-DMD$^{fl/fl}$ mice (Srivastava et al., 2000) and *Igf2r*$^{fl/fl}$ mice (Wylie et al.,
628 2003) by Prof. Bass Hassan (University of Oxford). Deletion of *H19*-DMD leads to reactivation of the
629 silent maternal *Igf2* allele, as well as down-regulation of *H19* mRNA levels (Srivastava et al., 2000).

630 All strains were bred into an inbred C57BL/6J genetic background for >10 generations, with the
631 exception of *Vav*^{iCre} strain that was maintained on an inbred C57BL/6N genetic background. For all
632 crosses (Table S5), the parent transmitting the floxed allele was also homozygous for the *Rosa26*
633 ^{fl}STOP^{fl}YFP allele. Thus, YFP expression provided an internal control for efficiency of Cre deletion (see
634 Figures S1, S3, S6 and S7). For all crosses fl/+ and +/fl as superscripts mean that the offspring has
635 inherited the floxed allele from the mother and father, respectively; Cre/+ and +/Cre as superscripts
636 mean that the offspring has inherited the Cre recombinase from the mother and father, respectively;
637 combination of fl/+, +/Cre means deletion of maternal floxed allele and combination of +/fl, Cre/+
638 means deletion of paternal floxed allele (see Table S5). Genotyping was performed by standard PCR
639 using DNA extracted from ear biopsies (adult mice) or tail DNA (fetuses). PCR was performed using

640 the Red Taq Ready PCR system (Sigma) (see list of primers in Table S6), followed by separation of PCR
641 amplicons by agarose gel electrophoresis.

642 **METHOD DETAILS**

643 **Plasma IGF2 measurements**

644 IGF2 measurements were performed with the Mouse IGF-II DuoSet ELISA kit (R&D Systems – DY792),
645 using an assay adapted for the MesoScale Discovery electrochemiluminescence immunoassay
646 platform (MSD). Briefly, MSD standard-bind microtitre plates were first coated with 30µl capture
647 antibody (Rat Anti-Mouse IGF-II, R&D Systems – 840962) diluted to 7.2 µg/ml in PBS, sealed, and
648 incubated overnight at 4°C. After three washes with MSD wash (0.1% Tween 20 in PBS), the plates
649 were loaded with 20µl ELISA Diluent RD5-38 per well, plus 10µl standard or plasma (diluted 50 fold in
650 RIPA buffer, Sigma – R0278). The plates were then sealed and incubated for two hours at room
651 temperature on a plate shaker. After three washes with MSD wash, the wells were plated with 25µl
652 detection antibody (Biotinylated Goat Anti-Mouse IGF-II, R&D Systems – 840963), diluted to 0.72
653 µg/ml in PBS, sealed, and incubated for one hour at room temperature on a plate shaker. Following
654 three additional washes with MSD wash, the wells were plated with 25µl MesoScale Discovery
655 Streptavidin Sulpho-TAG (MSD – R32AD-1), diluted 1:1000 in the MSD Diluent 100, sealed and
656 incubated for 30 minutes at room temperature on a plate shaker. After three final washes with MSD
657 wash, the wells were plated with 150µl of MSD Read Buffer T (1x) and the reading was performed on
658 the MSD s600 analyser. Each sample was measured in duplicate and the results were calculated
659 against the standard curve, using the MSD Workbench Software.

660 ***Igf2* mRNA *in situ* hybridization**

661 *In situ* hybridization was performed as described (Simmons et al., 2008), with minor modifications.
662 Briefly, a region of 415bp spanning *Igf2* coding exons 4-6 was PCR amplified using primers: 5'-
663 CACGCTTCAGTTTGTCTGTTCG-3' and 5'-GCTGGACATCTCCGAAGAGG-3' and E14 placental cDNA as
664 template. The PCR amplicon was cloned into a pCR2.1-TOPO plasmid (Thermo Fisher Scientific –
665 K450002). Sense (S) and antisense (AS) RNA probes were generated and labelled with Digoxigenin
666 (DIG) by *in vitro* reverse transcription, according to manufacturer's instructions (Roche –
667 11175025910). E14 fetuses and placentae were collected in ice-cold PBS and fixed overnight in 4%
668 paraformaldehyde in 0.1% diethylpyrocarbonate (DEPC)-PBS at 4°C. Tissues were then dehydrated
669 and embedded in paraffin, using RNase-free conditions. Tissue sections (7µm thick) mounted on
670 polysine slides were de-waxed, rehydrated in PBS, post-fixed in 4% paraformaldehyde for 10 minutes,
671 digested with proteinase K (30µg/ml) for 10 min at room temperature, acetylated for 10 minutes
672 (acetic anhydride, 0.25%) and hybridized overnight at 65°C in a humidified chamber with DIG-labeled
673 probes diluted in hybridization buffer. Two 65°C post-hybridization washes (1×SSC, 50% formamide,
674 0.1% tween-20) followed by two room temperature washes in 1×MABT were followed by 30 minutes
675 RNAse treatment. Sections were blocked for 1 hour in 1×MABT, 2% blocking reagent (Roche –
676 1096176001), 20% heat-inactivated goat serum and then incubated overnight with anti-DIG-AP
677 antibody (Roche – 11093274910; 1:2,500 dilution) at 4°C. After 4x20 min washes in 1×MABT, slides
678 were rinsed in 1×NTMT and incubated with BCIP/NBT mix in NTMT buffer, according to manufacturer's
679 instructions (Promega – S3771). Slides were counterstained with nuclear fast red, dehydrated, cleared
680 in xylene and mounted in DPX mounting medium. Pictures were taken with an Olympus DP71 bright-
681 field microscope fitted with a camera.

682 **Western blot analysis**

683 Tissues were lysed in ~10µl/mg tissue RIPA buffer (Sigma – R0278), then the lysates were spun at 3,000
684 RPM and 4°C for 15 minutes. The supernatants were transferred into new tubes and protein
685 concentrations were quantified using the Pierce BCA Assay Protein kit (Thermo Fisher Scientific –
686 23225). 60µg total protein were mixed with SDS gel loading buffer, then denatured at 70°C for 10
687 minutes and loaded into 12-well NuPAGE Novex 4-12% Bis-Tris precast gels (Thermo Fisher Scientific
688 – NP0322BOX). The pre-stained Novex Sharp protein standard (Invitrogen – LC5800) was used as
689 protein marker. After electrophoresis for 40 minutes at 200V and 4°C, the proteins were transferred
690 onto nitrocellulose membranes, using the iBlot Transfer Stacks (Invitrogen – IB3010-01) and the iBlot
691 Gel Transfer Device set for 7 minutes at 20V. Blocking was performed for one hour at 4°C in 5% semi-
692 skimmed milk (Marvel) dissolved in TBS-T. The membranes were then incubated overnight at 4°C with
693 the primary antibody dissolved in 0.5% milk in TBS-T (goat anti-human IGF2, 1:1,000, R&D Systems –
694 AF292-NA or goat anti-mouse SOD1, 1:50,000, R&D Systems – AF3787). After 2x10 minutes washes
695 with milliQ water and 2x10 minutes washes with TBS-T, the blots were incubated for one hour at room
696 temperature with the secondary antibody dissolved in TBS-T containing 3% semi-skimmed milk (rabbit
697 anti-goat IgG-HRP, 1:2,500, Santa Cruz sc-2768). The blots were then washed as above, exposed to
698 substrate (Clarity ECL Western Blotting Substrate, Bio-Rad – 1705060) for 5 minutes and imaged with
699 the Bio-Rad GelDoc system. Stripping of antibodies was carried out using a stripping buffer (Thermo
700 Fisher Scientific – 21059) for 15 minutes at room temperature. The band intensities were quantified
701 using the ImageLab software (Bio-Rad) and expressed as IGF2/SOD1 ratios.

702 **Placenta stereology**

703 Placenta stereology analyses for the *Igf2*^{EpiKO} and *Igf2*^{ECKO} models were performed as described (Coan
704 et al., 2004) in placentae (n=5–7) collected from three litters at each developmental stage. Briefly, the
705 placentae were weighted, then halved and each half placenta weighted again. A half was fixed in 4%
706 paraformaldehyde in PBS at 4°C overnight, then dehydrated and embedded in paraffin wax. The
707 paraffin blocks were exhaustively sectioned using a microtome at 7µm thickness. Placental sections
708 spaced 140 µm apart were hematoxylin-eosin stained and stereological measurements of placental
709 layers were done using the NewCAST system (Visiopharm, Hoersholm, Denmark), using the point
710 counting method (Coan et al., 2004).

711 The corresponding placental halves were fixed for 6 hours with 4% glutaraldehyde in 0.1 M PIPES
712 buffer, washed with 0.1 M PIPES buffer, and treated with 1% osmium tetroxide. The samples were
713 then resin-embedded and 1µm thick sections, obtained close to the placental midline, were stained
714 with methylene blue. Analysis of Lz components was done using the NewCAST system (Visiopharm)
715 with meander sampling of ~25% of the Lz area.

716 Placental stereology for *Igf2*^{HCKO} model was performed as described (De Clercq et al., 2020). Briefly,
717 placental samples were embedded in paraffin as described above, sectioned and then double-labelled
718 for lectin and cytokeratin, which allows the identification of Lz constituents. The proportion of FC, MBS
719 and LT was quantified using the NewCAST system and the point counting method, as described above.

720 **Transmission electron microscopy**

721 Analysis of E16 *Igf2*^{EpiKO} mutant and control placentae by transmission electron microscopy was
722 performed as previously described (Coan et al., 2005). Briefly, resin-embedded 1 µm thick sections,
723 cut near placental midline and stained with methylene blue as described in the previous section
724 (placenta stereology) were used to identify regions of interest. Thin sections (50 nm) were stained
725 with uranyl acetate and lead citrate, and viewed using a Philips CM100 transmission electron
726 microscope at 80 kV.

727 **Immunostainings**

728 Immunohistochemistry or immunofluorescence conditions are listed in Table S7. TUNEL staining was
729 performed using the In Situ Cell Death Detection Kit, TMR red (Sigma – 012156792910), or the TUNEL
730 Assay Kit – BrdU-Red (Abcam – ab66110) according to manufacturer's protocols. EdU staining was
731 done with the Click-iT EdU Alexa Fluor 488 Imaging Kit (Invitrogen – C10337), according to
732 manufacturer's instructions. For all immunofluorescence stains, DAPI (Sigma – D9542) was used to
733 label the nuclei. For all immunohistochemistry, images were taken with an Olympus DP71 bright-field
734 microscope. Immunofluorescence image acquisition was performed using a LSM510 Meta confocal
735 laser scanning microscope (Carl Zeiss, Jena, Germany) and the ZEN 2009 software or a SP8 laser-
736 scanning confocal microscope (Leica, Mannheim, Germany). Fluorescence semi-quantification
737 analysis was performed using Volocity 6.3 (Improvision). Counting of TUNEL$^+$ and F4/80$^+$ cells was
738 performed using HALO image analysis software (PerkinElmer).

739 **qRT-PCR analysis**

740 Total RNA was extracted using RNeasy Plus Kits (Qiagen – 74134 and 74034). RNA concentration was
741 measured by NanoDrop (Thermo Fisher Scientific) and quality was assessed in agarose gels. RNA
742 extracted from FACS isolated cells was quantified and assessed for quality using the RNA 6000 Pico Kit
743 (Agilent – 5067-1513) and an Agilent 2100 Bioanalyzer. Reverse transcription was performed using the
744 RevertAid RT Reverse Transcription Kit (Thermo Fisher Scientific – K1622). qRT-PCR was performed
745 with the SYBR Green JumpStart Taq Ready Mix (Sigma – S4438) and custom-made primers (Table S6)
746 using an ABI Prism 7900 system (Applied Biosystems). For gene expression normalization, we used
747 four housekeeping genes (*Gapdh*, *Sdha*, *Pmm1*, *Ppia*). Levels of expression were calculated using the
748 $2^{-\Delta\Delta Ct}$ method (Livak et al., 2001).

749 **Expression microarray analysis**

750 Total RNA was extracted from E19 male placental Lz using RNeasy Midi Kits (Qiagen – 75144) and
751 quantity and quality were verified using RNA 6000 Nano Kit (Agilent – 5067-1511) and an Agilent 2100
752 Bioanalyzer. Only RNA samples with RNA integrity numbers (RIN) >9.0 were used. Array profiling was
753 performed using the Mouse Gene 1.0 ST Array (Affymetrix – 901171) and the analysis of the data was
754 performed using GeneSpring GX 12.1 (Agilent, Santa Clara, CA, USA), with two algorithms: RMA
755 (Robust Multiarray Average) and PLIER (Probe Logarithmic Intensity Error). Only genes with $\log_2$ fold
756 change > 0.3 predicted by both algorithms were listed as DEGs. Pathway analysis was performed using
757 Ingenuity Pathway Analysis (version 2012).

758 **Flow cytometry analyses**

759 For flow cytometry analyses of FPEC, placental Lz samples were micro-dissected in ice-cold PBS. Tissue
760 dissociation into single cells was achieved by digestion at 37°C for 45 minutes with a 0.1% collagenase
761 P solution, aided by mechanical dissociation with needles of decreasing diameter. The cells were then
762 passed through 70-µm cell strainers and washed once in ice-cold PBS + 0.1% BSA. Erythrocytes were
763 lysed using the RBC lysis buffer (BioLegend – 420301). Pelleted cells were then re-suspended in 100µl
764 staining buffer (BioLegend – 420201), counted using the Cedex XS Analyser (Roche) and diluted at
765 1,000 cells/µl. Blocking of Fc receptors was performed by incubation at 4°C for 20 minutes with an
766 unlabelled anti-CD16/32 (1 µg/million cells; BioLegend – 101320). The cells were then incubated for
767 one hour at 4°C in the dark with a mix of rat anti-mouse CD41 (labelled with Phycoerythrin, PE)
768 (BioLegend – 133906; 0.25 µg per million cells), rat anti-mouse CD31 (labelled with AF647) (BioLegend
769 – 102516; 0.25 µg per million cells) and rat anti-mouse CD45 (labelled with V500) (BD Horizon –
770 561487; 0.4 µg per million cells) in 200µl staining buffer. Stained cells were washed twice in 1ml

771 staining buffer, re-suspended in PBS containing a viability marker (7-AAD – 7-Aminoactinomycin,
772 Invitrogen – A1310), filtered again through 70-µm cell strainers and incubated on ice for 5 minutes.
773 Flow cytometry analysis was performed with a BD FACSCantoII machine (BD Biosciences) and 100,000
774 events were recorded for each sample. FSC files were analysed with the FlowJo_V10 software, using
775 single-cell discrimination and gating based on single-stained controls. FPEC were identified as $7AAD^-$
776 $/CD31^+/CD41^-$ cells.

777 For flow cytometry analyses of $EPCAM^{high}$ positive cells, whole E12 placentae were dissociated into
778 single cells as described above. After erythrocyte lysis, cell counting and blocking of Fc receptors using
779 an unlabelled anti-CD16/32 antibody, cells were incubated for one hour at 4°C in the dark with AF647
780 rat anti-mouse CD326 (Epcam) antibody (BioLegend – 118212; 0.25 µg per million cells) in 200µl
781 staining buffer. Stained cells were washed as above, incubated with the viability marker 7-AAD and
782 filtered through 70-µm cell strainers. Flow cytometry analysis was performed with a BD FACSCantoII
783 machine (BD Biosciences) and FSC files were analysed with the FlowJo_V10 software, using single-cell
784 discrimination and gating based on single-stained controls.

785 **Flow cytometry analysis of FPEC proliferation**

786 Pregnant female mice received intraperitoneal (i.p.) injections with 50µg of 5-ethynyl-2'-deoxyuridine
787 (EdU)/g body weight (Thermo Fisher Scientific – A10044), 16 hours prior to tissue collection. Placental
788 Lz dissociation into single cells was performed as above. Cells re-suspended at a concentration of 1000
789 cells/µl were incubated for 30 minutes at 4°C with 1 µl Red LIVE/DEAD Fixable Dead Cell Stain (Thermo
790 Fisher Scientific – L23102). After one wash in PBS, the cells were pre-incubated for 20 minutes at 4°C
791 in the dark with unlabelled rat anti-mouse CD16/32 (BioLegend – 101320, 1 µg/million cells), then for
792 1 hour at 4°C in the dark with a 1:1 mix of rat anti-mouse CD41 (labelled with BV421) (BioLegend –
793 133911; 0.25 µg per million cells) and rat anti-mouse CD31 (labelled with AF647) (BioLegend – 102516;
794 0.25 µg per million cells) in staining buffer. After two washes with staining buffer, the cells were
795 stained using the Click-iT EdU Alexa Fluor 488 Flow Cytometry Assay Kit (Thermo Fisher Scientific –
796 C10420), according to manufacturer's instructions. Flow cytometry analysis was performed using a BD
797 LSRFortessa cell analyser (BD Biosciences). FSC files were analysed with the FlowJo_V10 software,
798 using single-cell discrimination and gating based on single-stained controls. Proliferating FPEC were
799 identified as viable $EdU^+/CD31^+/CD41^-$ cells.

800 **FPEC and HC isolation by FACS**

801 For sorting FPEC, single cell preparation and staining was performed as above. For sorting HC, entire
802 placentae collected at E13 were used for single cell preparation as described above. Single cell
803 suspensions were pre-incubated for 20 minutes at 4°C in the dark with unlabelled rat anti-mouse
804 CD16/32 (BioLegend – 101320, 1 µg/million cells), then stained for one hour at 4°C in the dark with a
805 mix of rat anti-mouse CD117/c-kit (labelled with PE) (BioLegend – 105808; 0.4 µg per million cells), rat
806 anti-mouse CD34 (labelled with AF700) (ThermoFisher Scientific – 56-0341-82; 1 µg per million cells),
807 rat anti-mouse Ly-6A/E (Sca1) (labelled with BV510) (BioLegend – 108129; 5 µl per million cells) and
808 rat anti-lineage cocktail (labelled with BV421) (BioLegend – 133311; 5 µl per million cells) in staining
809 buffer and washed twice. FACS was done using an Aria-Fusion cell sorter (BD Bioscience), with
810 exclusion of cell duplets and dying cells ($7AAD^+$). Cell fractions (endothelial, non-endothelial and
811 hematopoietic cells) were then spun at 3,000 RPM and 4°C for 3 min, the excess of sorting liquid was
812 removed and cell pellets were flash frozen in liquid nitrogen and stored at -80°C until used for RNA
813 extraction.

814 **Primary FPEC isolation, culture and tube formation assay**

815 Primary FPEC were isolated as previously described (Branco-Price et al., 2012) and adapted here to
816 placental Lz (E16). Briefly, placental Lz were micro-dissected on ice in RPMI containing 1%
817 penicillin/streptomycin. All samples from one litter were pooled, minced and digested for 90 minutes
818 at 37°C in 2 mg/ml collagenase type I (Sigma – SCR103) in HBSS containing 2mM CaCl2, 2mM MgSO4,
819 and 20mM HEPES. The digests were filtered through 70µm nylon cell strainers and washed in HBSS.
820 The cell pellets were then resuspended in PBS containing 0.1% BSA and incubated with anti-CD31-
821 coated magnetic beads for one hour at 4°C. Cells coated with beads were cultured in endothelial cell
822 growth medium consisting of low glucose DMEM:F12 with 1% nonessential amino acids, 2mM sodium
823 pyruvate, buffered with 20mM HEPES and supplemented with 20% FBS and 75µg/ml endothelial
824 mitogens (Sigma – E2759). The cells were incubated at 37°C in 5% O2 and 5% CO2. After four days, the
825 dead cells were washed and new media was added, additionally supplemented with 20µg/ml Heparin.
826 Sub-confluent cells (~80%) at passage one (around 10 days in culture) were washed and then cultured
827 in 5% serum replacement media (Sigma – S0638) for ~40 hours. From each litter we used cells at
828 passage one for treatment with 50 ng/ml mouse recombinant IGF2 (R&D Systems, 792-MG-050;
829 dissolved in PBS), 1000 ng/ml human $IGF2^{Leu27}$ (GroPep – TU100; dissolved in 10mM HCl), 500nM
830 picropodophyllotoxin (PPP, Sigma – T9576; dissolved in DMSO) or 500nM PPP + 50 ng/ml IGF2, or
831 appropriate vehicle control. The cells were harvested with Accutase (Sigma – A6964) and counted
832 using the ADAM™ Automated cell counter (NanoEnTek Inc) and 3,000 cells were seeded into 15-well
833 Angiogenesis µ-Slides (Ibidi – 81506) preloaded with 10µl matrigel/well (BD Biosciences – 354234).
834 Photographs were taken at 30 min, 4, 6 and 8 hours using an EVOS FL Cell Imaging system (Thermo
835 Fisher Scientific). Each experiment was performed on 5-6 litters for every treatment. For each tube
836 formation assay, we used five wells seeded with primary FPEC exposed to the treatment agent with
837 equivalent numbers of the corresponding vehicle. Quantification of tubular network structures was
838 performed using the Angiogenesis Analyzer software in ImageJ (Schneider et al., 2012).

839 **siRNA knockdown of *Igf2r***

840 Small interfering RNA (siRNA) knockdown of *Igf2r* was performed on primary placental microvascular
841 endothelial cells isolated from C57BL/6J mice (Cell Biologics, C57-6056) and grown in Cell Biologics'
842 complete growth medium (M1168) under standard culture conditions (37°C in 21% O2 and 5% CO2).
843 Endothelial cells were transfected with stealth siRNA for *Igf2r* or scrambled siRNA (Thermo Fisher
844 Scientific 1320003 and 12935100, respectively) using Lipofectamine RNAiMax transfection reagent
845 (Thermo Fisher Scientific 13778075).

846 The impact of *Igf2r* knockdown on endothelial cell proliferation rates, with or without exogenous IGF2
847 stimulation, was analysed using a previously described protocol (Woods et al., 2017). In brief, 10,000
848 endothelial cells transfected with either scrambled or *Igf2r* siRNA were plated in basal medium
849 (M1168b, which does not contain VEGF, ECGS, EGF and FBS) supplemented with hydrocortisone,
850 heparin and serum replacement (Sigma, S0638) in the presence or absence of 50 ng/ml recombinant
851 mouse IGF2 (R&D Systems, 792-MG-050), and collected every 24 hours over a period of four days. The
852 number of viable cells was counted using the Countess 3 Automated Cell Counter (Thermo Fisher
853 Scientific), according to manufacturer's instructions.

854 To study the impact of *Igf2r* knockdown on intracellular signalling pathways, following 48h of
855 transfection, cells were starved in the basal medium (M1168b) for 20h and then stimulated with
856 recombinant mouse IGF2 (50 ng/ml) and collected at the specific times (1, 5 and 10 min). Total cell
857 extracts were prepared in radioimmunoprecipitation assay buffer (20 mM Tris-HCl, pH 8.0, 137 mM
858 NaCl, 1 mM MgCl2, 1 mM CaCl2, 10% glycerol, 1% NP-40, 0.5% sodium deoxycholate, 0.1% sodium
859 dodecyl sulphate), containing a protease inhibitor cocktail (Sigma, P2714), and incubated at 4°C for
860 1 h. Western blotting was performed as previously described (Pérez-García et al., 2014). Blots were

861 probed with the following antibodies: rabbit anti IGF2R (Cell Signaling, 14364), mouse anti-Phospho-
862 p44/42 MAPK (Erk1/2) (Thr202/Tyr204) (Cell Signaling, 9106), rabbit anti-p44/42 MAPK (Erk1/2) (Cell
863 Signaling, 9102), rabbit anti-Phospho-Akt (Ser473) (Cell Signaling, 9271), rabbit anti-Akt (Cell Signaling,
864 9272), rabbit anti-HSP90 (Cell Signaling, 4877). Horseradish peroxidase-conjugated secondary
865 antibodies were from Bio-Rad. Detection was carried out with enhanced chemiluminescence reaction
866 (GE Healthcare, RPN2209) using standard X-ray films. Band intensities were quantified using ImageJ
867 software.

868 **RNA-sequencing and data analysis**

869 Total RNA was extracted from sorted FPEC by FACS from E16 male placentae using RNeasy Plus Micro
870 Kits (Qiagen – 74034). Quantity and quality were verified using the RNA 6000 Pico Kit (Agilent – 5067-
871 1513) and an Agilent 2100 Bioanalyzer. Only RNA samples with RNA integrity numbers (RIN) >9.0 were
872 used. Total RNA (2 ng) was whole-transcriptome amplified using the Ovation RNA–Seq System V2
873 (NuGEN). To prepare the RNA–seq libraries the amplified cDNA (2µg per sample) was fragmented to
874 200bp using a Bioruptor Sonicator (Diagenode), end repaired and barcoded using the Ovation Rapid
875 DR Library System (NuGEN). The libraries were combined and loaded onto an Illumina HiSeq 2500
876 system for single-end 50bp sequencing at the Genomics Core Facility, Cambridge Institute, CRUK. The
877 reads were aligned onto the mouse GRCm38 genome using TopHat 2.0.11 (Kim et al., 2013). Gene
878 abundance and differential expression were determined with Cufflinks 2.2.1 (Trapnell et al., 2010) and
879 expressed in fragments per kilobase per million mapped reads (FPKM). The cut off for expression was
880 set at ≥1 FPKM. Genes with a linear fold expression change greater than 1.5 and a Benjamini–Hochberg
881 false discovery rate (FDR) <5% were considered differentially expressed.

882 Functional analysis was performed using DAVID (Database for Annotation, Visualization and
883 Integrated Discovery; v6.8 http://david.abcc.ncifcrf.gov/). Enriched gene ontology (GO) terms with
884 FDR < 5% were considered significant. These terms were then clustered semantically using REViGO
885 (Reduce and Visualize GO) (Supek et al., 2011), which removes redundancy, and ordered according to
886 the $\log_{10}$ *P* values.

887 To search for enrichment of TF binding sites at the promoters of DEG, we used EPD (Eukaryotic
888 Promoter Database – https://epd.vital-it.ch/index.php) to retrieve the DNA sequences from 1,000bp
889 upstream to 100bp downstream of the transcriptional start site (TSS). These sequences were then
890 analysed using AME (Analysis of Motif Enrichment v4.12.0 – http://meme-suite.org/tools/ame) by
891 selecting *Mus musculus* and HOCOMOCO Mouse (v11 FULL) as motif database. Transcriptional
892 network visualization was performed using the Ingenuity Pathway Analysis tool.

893

894 **QUANTIFICATION AND STATISTICAL ANALYSIS**

895 No statistical analysis was used to predetermine sample size. Randomization was not used in our
896 animal studies. Placental stereology and histological EdU analyses were performed blinded to
897 genotype. Statistical analyses for fetus, placenta and Lz growth kinetics were performed in R, using a
898 mixed effects model, with litter as a random effect and genotype, developmental stage and the
899 interaction between genotype and developmental stage as fixed effects. Prior to these analyses, fetal,
900 placental and Lz weights were log transformed. All other statistical analyses were performed using
901 GraphPad Prism 8. Statistical significance between two groups was determined by Mann-Whitney
902 tests or two-tailed unpaired t-tests and statistical significance between multiple groups was
903 performed using one-way ANOVA plus Tukey's multiple comparisons tests or two-way ANOVA plus

904 Sidak's multiple comparisons tests, as appropriate. The numbers of samples or litters used for each
905 experiment are indicated in figure legends.

906

907 **REFERENCES**

908 1. Angiolillo, A.L., Sgadari, C., Taub, D.D., Liao, F., Farber, J.M., Maheshwari, S., Kleinman, H.K.,
909 Reaman, G.H., and Tosato, G. (1995). Human interferon-inducible protein 10 is a potent inhibitor
910 of angiogenesis in vivo. J. Exp. Med. *182*, 155–162.
911 2. Angiolini, E., Coan, P.M., Sandovici, I., Iwajomo, O.H., Peck, G., Burton, G.J., Sibley, C.P., Reik, W.,
912 Fowden, A.L., and Constância, M. (2011). Developmental adaptations to increased fetal nutrient
913 demand in mouse genetic models of Igf2-mediated overgrowth. FASEB J. 25, 1737–1745.
914 3. Aoki, A., Shiozaki, A., Sameshima, A., Higashimoto, K., Soejima, H., and Saito, S. (2011). Beckwith-
915 Wiedemann syndrome with placental chorangioma due to H19-differentially methylated region
916 hypermethylation: a case report. J. Obstet. Gynaecol. Res. *37*, 1872–1876.
917 4. Aplin, J.D., Myers, J.E., Timms, K., and Westwood, M. (2020). Tracking placental development in
918 health and disease. Nat. Rev. Endocrinol. *16*, 479–494.
919 5. Armes, J.E., McGown, I., Williams, M., Broomfield, A., Gough, K., Lehane, F., and Lourie, R. (2012).
920 The placenta in Beckwith-Wiedemann syndrome: genotype-phenotype associations, excessive
921 extravillous trophoblast and placental mesenchymal dysplasia. Pathology *44*, 519–527.
922 6. Augustin, H.G., Koh, G.Y., Thurston, G., and Alitalo, K. (2009). Control of vascular morphogenesis
923 and homeostasis through the angiopoietin-Tie system. Nat. Rev. Mol. Cell Biol. *10*, 165–177.
924 7. Austyn, J.M., and Gordon, S. (1981). F4/80, a monoclonal antibody directed specifically against
925 the mouse macrophage. Eur. J. Immunol. *11*, 805–815.
926 8. Azzi, S., Abi Habib, W., and Netchine, I. (2014). Beckwith-Wiedemann and Russell-Silver
927 Syndromes: from new molecular insights to the comprehension of imprinting regulation. Curr.
928 Opin. Endocrinol. Diabetes Obes. *21*, 30–38.
929 9. Bach, L.A. (2015). Endothelial cells and the IGF system. J. Mol. Endocrinol. *54*, R1–R13.
930 10. Baker, J., Liu, J.P., Robertson, E.J., and Efstratiadis, A. (1993). Role of insulin-like growth factors
931 in embryonic and postnatal growth. Cell *75*, 73–82.
932 11. Barlow, D.P., Stoeger, R., Herrmann, B.G., Sito, K., and Schweifer, N. (1991). The mouse insulin-
933 like growth factor type-2 receptor is imprinted and closely linked to the Tme locus. Nature *349*,
934 84–87.
935 12. Beukers, M.W., Oh, Y., Zhang, H., Ling, N., and Rosenfeld, R.G. (1991). [Leu27] insulin-like growth
936 factor II is highly selective for the type-II IGF receptor in binding, cross-linking and thymidine
937 incorporation experiments. Endocrinology *128*, 1201–1203.
938 13. de Boer, J., Williams, A., Skavdis, G., Harker, N., Coles, M., Tolaini, M., Norton, T., Williams, K.,
939 Roderick, K., Potocnik, A.J., et al. (2003). Transgenic mice with hematopoietic and lymphoid
940 specific expression of Cre. Eur. J. Immunol. *33*, 314–325.
941 14. Branco-Price, C., Zhang, N., Schnelle, M., Evans, C., Katschinski, D.M., Liao, D., Ellies, L., and
942 Johnson, R.S. (2012). Endothelial cell HIF-1α and HIF-2α differentially regulate metastatic success.
943 Cancer Cell *21*, 52–65.
944 15. Burns, J.L., and Hassan, A.B. (2001). Cell survival and proliferation are modified by insulin-like
945 growth factor 2 between days 9 and 10 of mouse gestation. Development *128*, 3819–3830.
946 16. Coan, P.M., Ferguson-Smith, A.C., and Burton, G.J. (2004). Developmental dynamics of the
947 definitive mouse placenta assessed by stereology. Biol. Reprod. *70*, 1806–1813.
948 17. Coan, P.M., Ferguson-Smith, A.C., and Burton, G.J. (2005). Ultrastructural changes in the
949 interhaemal membrane and junctional zone of the murine chorioallantoic placenta across
950 gestation. J. Anat. *207*, 783–796.

951 18. Coan, P.M., Fowden, A.L., Constância, M., Ferguson-Smith, A.C., Burton, G.J., and Sibley, C.P.
952 (2008). Disproportional effects of Igf2 knockout on placental morphology and diffusional
953 exchange characteristics in the mouse. J Physiol. *586*, 5023–5032.
954 19. Constância, M., Angiolini, E., Sandovici, I., Smith, P., Smith, R., Kelsey, G., Dean, W., Ferguson-
955 Smith, A., Sibley, C.P., Reik, W., et al. (2005). Adaptation of nutrient supply to fetal demand in the
956 mouse involves interaction between the Igf2 gene and placental transporter systems. Proc. Natl.
957 Acad. Sci. USA *102*, 19219–19224.
958 20. Constância, M., Hemberger, M., Hughes, J., Dean, W., Ferguson-Smith, A., Fundele, R., Stewart,
959 F., Kelsey, G., Fowden, A., Sibley, C., et al. (2002). Placental-specific IGF-II is a major modulator of
960 placental and fetal growth. Nature *417*, 945-948.
961 21. Constância, M., Kelsey, G., and Reik, W. (2004). Resourceful imprinting. Nature *432*, 53–57.
962 22. Davies, K., Bowden, L., Smith, P., Dean, W., Hill, D., Furuumi, H., Sasaki, H., Cattanach, B., and
963 Reik, W. (2002). Disruption of mesodermal enhancers for Igf2 in the minute mutant.
964 Development *129*, 1657–68.
965 23. De Clercq, K., Lopez-Tello, J., Vriens, J., and Sferruzzi-Perri, A.N. (2020). Double-label
966 immunohistochemistry to assess labyrinth structure of the mouse placenta with stereology.
967 Placenta *94*, 44–47.
968 24. DeChiara, T.M., Robertson, E.J., and Efstratiadis, A. (1991). Parental imprinting of the mouse
969 insulin-like growth factor II gene. Cell *64*, 849–859.
970 25. Dietrich, P., Dragatsis, I., Xuan, S., Zeitlin, S., and Efstratiadis, A. (2000). Conditional mutagenesis
971 in mice with heat shock promoter-driven cre transgenes. Mamm. Genome *11*, 196–205.
972 26. El-Shewy, H.M., Johnson, K.R., Lee, M.H., Jaffa, A.A., Obeid, L.M., and Luttrell, L.M. (2006). Insulin-
973 like growth factors mediate heterotrimeric G protein-dependent ERK1/2 activation by
974 transactivating sphingosine 1-phosphate receptors. J. Biol. Chem. *281*, 31399–31407.
975 27. El-Shewy, H.M., Lee, M.H., Obeid, L.M., Jaffa, A.A., and Luttrell, L.M. (2007). The insulin-like
976 growth factor type 1 and insulin-like growth factor type 2/mannose-6-phosphate receptors
977 independently regulate ERK1/2 activity in HEK293 cells. J. Biol. Chem. *282*, 26150–26157.
978 28. Ferrón, S.R., Radford, E.J., Domingo-Muelas, A., Kleine, I., Ramme, A., Gray, D., Sandovici, I.,
979 Constancia, M., Ward, A., Menheniott, T.R., et al. (2015). Differential genomic imprinting
980 regulates paracrine and autocrine roles of IGF2 in mouse adult neurogenesis. Nat. Commun. *6*,
981 8265.
982 29. Fehniger, T.A., and Caligiuri, M.A. (2001). Interleukin 15: biology and relevance to human disease.
983 Blood *97*, 14–32.
984 30. Fischer, A., Schumacher, N., Maier, M., Sendtner, M., and Gessler, M. (2004). The Notch target
985 genes Hey1 and Hey2 are required for embryonic vascular development. Genes Dev. *18*, 901–
986 911.
987 31. Fowden, A.L., Ward, J.W., Wooding, F.P., Forhead, A.J., and Constância, M. (2006). Programming
988 placental nutrient transport capacity. J. Physiol. *572*, 5–15.
989 32. Gardner, R.L., Squire, S., Zaina, S., Hills, S., and Graham, C.F. (1999). Insulin-like growth factor-2
990 regulation of conceptus composition: effects of the trophectoderm and inner cell mass
991 genotypes in the mouse. Biol. Reprod. *60*, 190–195.
992 33. Girnita, A., Girnita, L., del Prete, F., Bartolazzi, A., Larsson, O., and Axelson, M. (2004).
993 Cyclolignans as inhibitors of the insulin-like growth factor-1 receptor and malignant cell growth.
994 Cancer Res. *64*, 236–242.
995 34. Gohlke, B.C., Fahnenstich, H., Dame, C., and Albers, N. (2004). Longitudinal data for intrauterine
996 levels of fetal IGF-I and IGF-II. Horm. Res. *61*, 200–204.
997 35. Gregory, J.L., Morand, E.F., McKeown, S.J., Ralph, J.A., Hall, P., Yang, Y.H., McColl, S.R., and
998 Hickey, M.J. (2006). Macrophage migration inhibitory factor induces macrophage recruitment via
999 CC chemokine ligand 2. J. Immunol. *177*, 8072–8079.

1000 36. Ghosh, P., Dahms, N.M., and Kornfeld, S. (2003). Mannose 6-phosphate receptors: new twists in
1001 the tale. Nat. Rev. Mol. Cell Biol. *4*, 202–212.
1002 37. Hammerle, C.M., Sandovici, I., Brierley, G.V., Smith, N.M., Zimmer, W.E., Zvetkova, I., Prosser,
1003 H.M., Sekita, Y., Lam, B.Y.H., Ma, M., et al. (2020). Mesenchyme-derived IGF2 is a major paracrine
1004 regulator of pancreatic growth and function. PLoS Genet. *16*, e1009069.
1005 38. Harris, L.K., and Westwood, M. (2012). Biology and significance of signalling pathways activated
1006 by IGF-II. Growth Factors *30*, 1–12.
1007 39. Hughes, J., Surakhy, M., Can, S., Ducker, M., Davies, N., Szele, F., Bühnemann, C., Carter, E., Trikin,
1008 R., Crump, M.P., et al. (2019). Maternal transmission of an Igf2r domain 11: IGF2 binding mutant
1009 allele (Igf2rI1565A) results in partial lethality, overgrowth and intestinal adenoma progression.
1010 Sci. Rep. *6*, 11388.
1011 40. Hughes, M., Natale, B.V., Simmons, D.G., and Natale, D.R. (2013). Ly6e expression is restricted to
1012 syncytiotrophoblast cells of the mouse placenta. Placenta *34*, 831–835.
1013 41. Kappou, D., Sifakis, S., Konstantinidou, A., Papantoniou, N., and Spandidos, D.A. (2015). Role of
1014 the angiopoietin/Tie system in pregnancy (Review). Exp. Ther. Med. 9, 1091–1096.
1015 42. Keniry, A., Oxley, D., Monnier, P., Kyba, M., Dandolo, L., Smits, G., and Reik W. (2012). The H19
1016 lincRNA is a developmental reservoir of miR-675 that suppresses growth and Igf1r. Nat. Cell Biol.
1017 14, 659-665.
1018 43. Kim, D., Pertea, G., Trapnell, C., Pimentel, H., Kelley, R., and Salzberg, S.L. (2013).TopHat2:
1019 accurate alignment of transcriptomes in the presence of insertions, deletions and gene fusions.
1020 Genome Biol. *14*, R36.
1021 44. Kisanuki, Y.Y., Hammer, R.E., Miyazaki, J., Williams, S.C., Richardson, J.A., and Yanagisawa, M.
1022 (2001). Tie2-Cre transgenic mice: a new model for endothelial cell-lineage analysis in vivo. Dev.
1023 Biol. *230*, 230–242.
1024 45. Lankhorst, S., Danser, A.H., and van den Meiracker, A.H. (2016). Endothelin-1 and
1025 antiangiogenesis. Am. J. Physiol. Regul. Integr. Comp. Physiol. *310*, R230–R234.
1026 46. Lau, M.M., Stewart, C.E., Liu, Z., Bhatt, H., Rotwein, P., and Stewart, C.L. (1994). Loss of the
1027 imprinted IGF2/cation-independent mannose 6-phosphate receptor results in fetal overgrowth
1028 and perinatal lethality. Genes Dev. *8*, 2953–2963.
1029 47. Lawler, P.R., and Lawler, J. (2012). Molecular basis for the regulation of angiogenesis by
1030 thrombospondin-1 and -2. Cold Spring Harb. Perspect. Med. *2*, a006627.
1031 48. Lee, N.V., Sato, M., Annis, D.S., Loo, J.A., Wu, L., Mosher, D.F., and Iruela-Arispe, M.L. (2006).
1032 ADAMTS1 mediates the release of antiangiogenic polypeptides from TSP1 and 2. EMBO J. *25*,
1033 5270–5283.
1034 49. Livak, K.J., and Schmittgen, T.D. (2001). Analysis of relative gene expression data using real-time
1035 quantitative PCR and the 2(-Delta Delta C(T)) Method. Methods *25*, 402–408.
1036 50. Madisen, L., Zwingman, T.A., Sunkin, S.M., Oh, S.W., Zariwala, H.A., Gu, H., Ng, L.L., Palmiter, R.D.,
1037 Hawrylycz, M.J., Jones, A.R., et al. (2010). A robust and high-throughput Cre reporting and
1038 characterization system for the whole mouse brain. Nat. Neurosci. *13*, 133–140.
1039 51. Maeng, Y.S., Choi, H.J., Kwon, J.Y., Park, Y.W., Choi, K.S., Min, J.K., Kim, Y.H., Suh, P.G., Kang, K.S.,
1040 Won, M.H., et al. (2009). Endothelial progenitor cell homing: prominent role of the IGF2-IGF2R-
1041 PLCbeta2 axis. Blood *113*, 233–243.
1042 52. Mayhew, T.M., Charnock-Jones, D.S., and Kaufmann, P. (2004). Aspects of human fetoplacental
1043 vasculogenesis and angiogenesis. III. Changes in complicated pregnancies. Placenta *25*, 127–139.
1044 53. Miner, J.H., Cunningham, J., and Sanes, J.R. (1998). Roles for laminin in embryogenesis:
1045 Exencephaly, syndactyly, and placentopathy in mice lacking the laminin α5 chain. J. Cell Biol. *143*,
1046 1713–1723.

1047 54. Monk, D., Arnaud, P., Apostolidou, S., Hills, F.A., Kelsey, G., Stanier, P., Feil, R., and Moore, G.E.
1048 (2006). Limited evolutionary conservation of imprinting in the human placenta. Proc. Natl. Acad.
1049 Sci. USA *103*, 6623–6628.
1050 55. Nagai, A., Takebe, K., Nio-Kobayashi, J., Takahashi-Iwanaga, H., and Iwanaga, T. (2010). Cellular
1051 expression of the monocarboxylate transporter (MCT) family in the placenta of mice. Placenta
1052 *31*, 126–133.
1053 56. Okamoto, T., Katada, T., Murayama, Y., Ui, M., Ogata, E., and Nishimoto, I. (1990). A simple
1054 structure encodes G protein-activating function of the IGF-II/mannose 6-phosphate receptor. Cell
1055 *62*, 709–717.
1056 57. Oudejans, C.B., Westerman, M.B., Wouters, D., Gooyer, S., Leegwater, P.A., van Wijk, I.J., and
1057 Sleutels, F. (2001). Allelic IGF2R Repression Does Not Correlate with Expression of Antisense RNA
1058 in Human Extraembryonic Tissues. Genomics *73*, 331–337.
1059 58. Pérez-García, V., Redondo-Muñoz, J., Kumar, A., and Carrera, A.C. (2014). Cell activation-induced
1060 phosphoinositide 3-kinase alpha/beta dimerization regulates PTEN activity. Mol. Cell. Biol. *34*,
1061 3359–3373.
1062 59. Rawn, S.M., and Cross, J.C. (2008). The evolution, regulation, and function of placenta-specific
1063 genes. Annu. Rev. Cell. Dev. Biol. *24*, 159–181.
1064 60. Rhodes, K.E., Gekas, C., Wang, Y., Lux, C.T., Francis, C.S., Chan, D.N., Conway, S., Orkin, S.H.,
1065 Yoder, M.C., and Mikkola, H.K. (2008). The emergence of hematopoietic stem cells is initiated in
1066 the placental vasculature in the absence of circulation. Cell Stem Cell *2*, 252–263.
1067 61. Schneider, C.A., Rasband, W.S., and Eliceiri, K.W. (2012). NIH Image to ImageJ: 25 years of image
1068 analysis. Nat. Methods *9*, 671–675.
1069 62. Schwenk, F., Baron, U., and Rajewsky, K. (1995). A cre-transgenic mouse strain for the ubiquitous
1070 deletion of loxP-flanked gene segments including deletion in germ cells. Nucleic Acids Res. *23*,
1071 5080–5081.
1072 63. Sferruzzi-Perri, A.N., Sandovici, I., Constância, M., and Fowden, A.L. (2017). Placental phenotype
1073 and the insulin-like growth factors: resource allocation to fetal growth. J. Physiol. *595*, 5057–
1074 5093.
1075 64. Simmons, D.G., Rawn, S., Davies, A., Hughes, M., and Cross, J.C. (2008). Spatial and temporal
1076 expression of the 23 murine Prolactin/Placental Lactogen-related genes is not associated with
1077 their position in the locus. BMC Genomics *9*, 352.
1078 65. Srinivas, S., Watanabe, T., Lin, C.S., William, C.M., Tanabe, Y., Jessell, T.M., and Costantini, F.
1079 (2001). Cre reporter strains produced by targeted insertion of EYFP and ECFP into the ROSA26
1080 locus. BMC Dev. Biol. *1*, 4.
1081 66. Srinivasan, R., Zabuawala, T., Huang, H., Zhang, J., Gulati, P., Fernandez, S., Karlo, J.C., Landreth,
1082 G.E., Leone, G., and Ostrowski, M.C. (2009). Erk1 and Erk2 regulate endothelial cell proliferation
1083 and migration during mouse embryonic angiogenesis. PLoS One. *4*, e8283.
1084 67. Srivastava, M., Hsieh, S., Grinberg, A., Williams-Simons, L., Huang, S.P., and Pfeifer, K. (2000). H19
1085 and Igf2 monoallelic expression is regulated in two distinct ways by a shared cis acting regulatory
1086 region upstream of H19. Genes Dev. *14*, 1186–1195.
1087 68. Supek, F., Bošnjak, M., Škunca, N., and Šmuc, T. (2011). REVIGO summarizes and visualizes long
1088 lists of gene ontology terms. PLoS One *6*, e21800.
1089 69. Tallquist, M.D., and Soriano, P. (2000). Epiblast-restricted Cre expression in MORE mice: a tool to
1090 distinguish embryonic vs. extra-embryonic gene function. Genesis *26*, 113–115.
1091 70. Trapnell, C., Williams, B.A., Pertea, G., Mortazavi, A., Kwan, G., van Baren, M.J., Salzberg, S.L.,
1092 Wold, B.J., Pachter, L. (2010). Transcript assembly and quantification by RNA-seq reveals
1093 unannotated transcripts and isoform switching during cell differentiation. Nat. Biotechnol. *28*,
1094 511–515.

1095 71. Tzschoppe, A., Riedel, C., von Kries, R., Struwe, E., Rascher, W., Dörr, H.G., Beckmann, M.W.,
1096 Schild, R.L., Goecke, T.W., Flyvbjerg, A., et al. (2015). Differential effects of low birthweight and
1097 intrauterine growth restriction on umbilical cord blood insulin-like growth factor concentrations.
1098 Clin. Endocrinol. (Oxf). *83*, 739–745.
1099 72. Ueno, M., Lee, L.K., Chhabra, A., Kim, Y.J., Sasidharan, R., Van Handel, B., Wang, Y., Kamata, M.,
1100 Kamran, P., Sereti, K.I., et al. (2013). c-Met-dependent multipotent labyrinth trophoblast
1101 progenitors establish placental exchange interface. Dev. Cell. *27*, 373–386.
1102 73. Uthaiah, R.C., Praefcke, G.J., Howard, J.C., and Herrmann, C. (2003). IIGP1, an interferon-gamma-
1103 inducible 47-kDa GTPase of the mouse, showing cooperative enzymatic activity and GTP-
1104 dependent multimerization. J. Biol. Chem. *278*, 29336–29343.
1105 74. Verhaeghe, J., Van Bree, R., Van Herck, E., Laureys, J., Bouillon, R., and Van Assche, F.A. (1993).
1106 C-peptide, insulin-like growth factors I and II, and insulin-like growth factor binding protein-1 in
1107 umbilical cord serum: correlations with birth weight. Am. J. Obstet. Gynecol. *169*, 89–97.
1108 75. Vidal, A., and Koff, A. (2000). Cell-cycle inhibitors: three families united by a common cause. Gene
1109 *247*, 1–15.
1110 76. Wang, Z.Q., Fung, M.R., Barlow, D.P., and Wagner, E.F. (1994). Regulation of embryonic growth
1111 and lysosomal targeting by the imprinted Igf2/Mpr gene. Nature *372*, 464-467.
1112 77. Wei, Y., Su, J., Liu, H., Lv, J., Wang, F., Yan, H., Wen, Y., Liu, H., Wu, Q., and Zhang, Y. (2014).
1113 MetaImprint: an information repository of mammalian imprinted genes. Development *141*,
1114 2516–2523.
1115 78. Wenzel, P.L., and Leone, G. (2007). Expression of Cre recombinase in early diploid trophoblast
1116 cells of the mouse placenta. Genesis *45*, 129–134.
1117 79. Woods, L., Perez-Garcia, V., Kieckbusch, J., Wang, X., DeMayo, F., Colucci, F., and Hemberger, M.
1118 (2017). Decidualisation and placentation defects are a major cause of age-related reproductive
1119 decline. Nat. Commun. *8*, 352.
1120 80. Wylie, A.A., Pulford, D.J., McVie-Wylie, A.J., Waterland, R.A., Evans, H.K., Chen, Y.T., Nolan, C.M.,
1121 Orton, T.C., and Jirtle, R.L. (2003). Tissue-specific inactivation of murine M6P/IGF2R. Am. J.
1122 Pathol. *162*, 321–328.
1123 81. Xu, Y., Goodyer, C.G., Deal, C., Polychronakos, C. (1993). Functional polymorphism in the parental
1124 imprinting of the human IGF2R gene. Biochem. Biophys. Res. Commun. *197*, 747–754.
1125 82. Yamazawa, K., Kagami, M., Nagai, T., Kondoh, T., Onigata, K., Maeyama, K., Hasegawa, T.,
1126 Hasegawa, Y., Yamazaki, T., Mizuno, S., et al. (2008). Molecular and clinical findings and their
1127 correlations in Silver-Russell syndrome: implications for a positive role of IGF2 in growth
1128 determination and differential imprinting regulation of the IGF2-H19 domain in bodies and
1129 placentas. J. Mol. Med. *86*, 1171–1181.
1130 83. Ziegler, A.N., Feng, Q., Chidambaram, S., Testai, J.M., Kumari, E., Rothbard, D.E., Constancia, M.,
1131 Sandovici, I., Cominski, T., Pang, K., et al. (2019). Insulin-like Growth Factor II: An Essential Adult
1132 Stem Cell Niche Constituent in Brain and Intestine. Stem Cell Reports *12*, 816-830.